Università Politecnica delle Marche
Dottorato di Ricerca in Scienze dell'Ingegneria
Curriculum "Ingegneria Biomedica, Elettronica e delle Telecomunicazioni"

Development of an electromagnetic model to characterize the field diffracted by a human body for AAL applications

Ph.D. Dissertation of:
Giovanni Manfredi

Advisor:
Prof. Graziano Cerri

Curriculum Supervisor:
Prof. Franco Chiaraluce

XV edition - new series

Università Politecnica delle Marche
Dottorato di Ricerca in Scienze dell'Ingegneria
Curriculum "Ingegneria Biomedica, Elettronica e delle Telecomunicazioni"

Development of an electromagnetic model to characterize the field diffracted by a human body for AAL applications

Ph.D. Dissertation of:
Giovanni Manfredi

Advisor:
Prof. Graziano Cerri

Curriculum Supervisor:
Prof. Franco Chiaraluce

XV edition - new series

Università Politecnica delle Marche
Dottorato di Ricerca in Scienze dell'Ingegneria
Facoltà di Ingegneria
Via Brecce Bianche – 60131 Ancona (AN), Italy

To my family and Alessandra

«Logic will get you from A to B.
Imagination will take you everywhere.»
Albert Einstein

alla mia famiglia e ad Alessandra

« La logica ti può portare da A a B.
L'immaginazione invece ti può portare ovunque.

Acknowledgments

The making of this dissertation would have been impossible without the support from numerous people I encountered throughout my educational, professional, and personal life.
First of all, I would like to express my deepest appreciation and gratitude to my supervisor Prof. Graziano Cerri, for his teaching and guidance which become my source of inspiration and motivation. I wish to express my gratitude to Ing. Alfredo De Leo, Ing. Paola Russo and Ing. Lorenzo Scalise for their helpful suggestions during my research work. I would like to thank my office colleagues Valentina Di Mattia, Marco Pieralisi, Valerio Petrini and Luca Bastianelli for their support, patience and encouragement during my research.
My sincere appreciation also goes to Director of SONDRA Lab Marc Lesturgie who gave me the opportunity to work with his research group. A special thank to my supervisor Laetitia Thirion-Lefevre and to SONDRA research team - Jean-Philippe Ovarlez, Israel Hinostroza, Thierry Letertre and Régis Guinvarc'h - for their full support and insightful comments which helped to improve the quality of this work.
I would also thank the colleagues of Automation research group with particular regard Luca Cavanini for his friendship, support and moments of fun.
Most of all, I would like to thank my family for their constant support and understanding, and Alessandra for her love, encouragement and support throughout the development of this dissertation and my entire Ph.D years, to whom I dedicate my work.

Ancona, November 2016

Giovanni Manfredi

Abstract

The research presented in this thesis regards the development and implementation of an analytical model, for the characterisation of the fields diffracted by a human body, for AAL (*Ambient Assisted Living*) applications. In the recent years there was growing demand for contact-less sensors addressed to remote monitoring of vital signs, in order to improve the patients' quality of life.

This kind of systems entails the use of electromagnetic (EM) technology, and their proper design involves the analysis of the interaction between a human body and an electromagnetic wave. EM commercial tools are able to characterise this interaction, but they require a huge memory consumption and a great amount of time computation.

To this purpose, an EM model based on the physical optics (PO) approach is presented in this thesis, where a human body was reproduced by homogenous canonical shapes. The analytical model proves to be reliable and sufficiently accurate, reducing the computational burden required by PO-based ray tracing implemented in commercial software.

Measurements and simulations with the EM model, implemented in MATLAB, were performed and compared, to test its accuracy and feasibility, considering a metallic sphere, lossless homogeneous objects (sphere and cylinder), and dielectric complex structures (mannequin and real target). In addition, radar Doppler techniques are studied and implemented in the proposed model, in order to analyse and discriminate general activities of a monitored moving target. The use of the EM model allows to optimise the design of unobtrusive sensors, for the remote monitoring of the vital signs, the falls detection and the energy expenditure of physical activities of elderly people in indoor environments.

Sommario

Il lavoro di ricerca presentato in questa tesi riguarda lo sviluppo e l'implementazione di un modello analitico, per la caratterizzazione dei campi diffratti da un corpo umano, per applicazioni nell'ambito del *Ambient Assisted Living (AAL)*.
Negli ultimi anni c'è stata una crescente domanda di sensori senza contatto destinati al monitoraggio da remoto dei parametri vitali, al fine di migliorare la qualità di vita dei pazienti.
Questo tipo di sistemi prevede l'utilizzo di una tecnologia basata sulla propagazione di onde elettromagnetiche, e la loro corretta progettazione prevede l'analisi dell'interazione tra corpo umano e onda EM. Programmi di simulazione elettromagnetica sono in grado di caratterizzare tale interazione, ma richiedono un consumo di memoria enorme e una grande quantità di tempo di calcolo. Invece, un modello analitico riduce l'onere computazionale, e si dimostra affidabile e sufficientemente accurato.
A tale scopo, un modello EM basato su un approccio di tipo ottica-fisica è presentato in questa tesi, in cui il corpo umano è stato riprodotto mediante forme canoniche omogenee. Misure e simulazioni effettuate con il modello EM, implementato in MATLAB, sono stati eseguite e confrontate, per analizzare l'accuratezza e la fattibilità del modello analitico, considerando una sfera metallica, oggetti omogenei senza perdite (sfera e cilindro), e strutture complesse dielettriche (manichino e target reale). Inoltre, tecniche di radar Doppler sono state studiate e implementate nel modello, al fine di analizzare e discriminare attività generali di un target in movimento. Il modello EM permette di ottimizzare la progettazione di sensori senza contatto, per il monitoraggio da remoto dei parametri vitali, per il rilevamento di cadute e della spesa energetica relativa ad attività fisiche di persone anziane in ambienti chiusi.

Acronyms

AAL Ambient Assisted Living

EM Electromagnetic

ETA Electronic Travel Aids

EOA Electronic Orientation Aids

RR Respiratory Rythm

CW Continuous Wave

UWB Ultra Wide Band

WBAN Wireless Body Area Network

CST MWS CST MICROWAVE STUDIO

FDTD Finite Difference Time Domain

MoM Method of Moments

GO Geometric Optics

PO Physical Optics

PTD Physical Theory of Diffraction

SAM Specific Anthropomorphic Mannequin

RCS Radar Cross Section

PEC Perfect Electric Conductor

STFT Short-Time Fourier Transform

FMM Fast Multipole Method

SONDRA Supelec Onera NUS DSO Research Alliance

FFT Fast Fourier Transform

IFT Inverse Fourier Transform

VNA Vectorial Network Analyser

FoPen Foliage Penetration

GPR Ground Penetrating Radar

Contents

List of Figures

List of Tables

Chapter 1.

Summary of Ph.D. Research Activity

The aim of this chapter is to present the main activities that I performed during my Ph.D. in the triennium 2014-2016, in collaboration with the research group of Antenna Laboratory of Department of Information Engineering at UNIVPM. The research was focused on three main topics:

- Design and realisation of EM devices for safe mobility of visually impaired people;
- Design and realisation of contact-less sensors for remote monitoring of physiological activities of a subject in indoor environment;
- Development of analytical model to characterise the fields reflected by a human body for *Ambient Assisting Living (AAL)* applications.

Those activities are summarised in the following sections.

1.1. Electromagnetic aids for visually impaired people

The traditional aids for the mobility of blind people are the long (*white*) cane and the guide dog. For some years, different kinds of electronic aids have appeared to prevent blind people from walking into obstacles (*Electronic Travel Aids (ETA)*) or to help them to find their way (*Electronic Orientation Aids (EOA)*). Nevertheless, in literature, there is a lack of studies, which consider electromagnetic (*EM*) radiation as the physical quantity able to deliver information on an obstacle presence for visually impaired people. Therefore, in these years, the main aim was to investigate the capability of novel EM systems designed for visually impaired and blind user mobility. An obstacle detection

system was designed (*EM Cane*), to aid visually impaired users to walk safely and independently. The proposed approach provides additional information on obstacles (height from the ground, distance and position of the obstacle) in comparison with the available assistive technologies currently used. The EM cane was tested by a blind person and it is shown in the online video `http://youtu.be/4k9wz72XlNE`.

Other studies investigated the possibility to improve the performances of blind athletes, in particular marathon runners, using electromagnetic systems. These EM devices (*Track for virtual line* and *Active athletics track*) are addressed to make the blind athlete free of running independently from his guide, at least during training sessions. The first system creates a invisible hallway by means of two transmitting antennas located on a vehicle running in front of the athlete. Whenever the runner gets close to one of the two borderlines, a wearable receiver, located on the user's chest, indicates him to move toward the central position, through two vibrating transducers positioned on his left and right arm (`http://youtu.be/GIyQDuOnOww`). The second system generates two magnetic fields with the use of two wires placed on the ground of an athletics track. The current flowing in each wire generates a magnetic field, whose flux variation depends on relative position, between the athlete and the wire, and it is sensed by a receiver worn by the runner. The generation of the warning signals is the same adopted in the previous EM device.

My contributions concerned about:

- the analysis of the performed measurements for the characterization of the radiation pattern of the designed and simulated antennas;

- the setting up of tests about the realised prototypes with the blind user.

The detailed descriptions of the presented systems are available in the follow publications:

- Journal
  - M. Pieralisi, V. Petrini, V. Di Mattia, G. Manfredi, A. De Leo, L. Scalise, P. Russo, G. Cerri, *Design and Realisation of an Electromagnetic Guiding System for Blind Running Athletes*, Sensors (Basel), 2015 Jul 8;15(7):16466-83

- Conference Proceeding
  - V. Di Mattia, A. Caddemi, E. Cardillo, G. Manfredi, A. De Leo, P. Russo, L. Scalise, G. Cerri, *A Feasibility Study of a Compact*

Radar System for Autonomous Walking of Blind People, 2016 IEEE 2nd International Forum on Research and Technologies for Society and Industry Leveraging a better tomorrow (RTSI), 6-9 Sept. 2016, Bologna (Italy).

- V. Di Mattia, V. Petrini, M. Pieralisi, G. Manfredi, A. De Leo, P. Russo, L. Scalise And G. Cerri, *A K-Band miniaturised antenna for safe mobility of visually impaired people*, Microwave Symposium (MMS), 2015 IEEE 15th Mediterranean, Lecce, 2015, pp. 1-4.

- G. Cerri, A. De Leo, V. Di Mattia, G. Manfredi, V. Mariani Primiani, V. Petrini, M. Pieralisi, P. Russo, L. Scalise, *The electromagnetic technology for safe mobility of visually impaired people*, Control and Automation (MED), 2014 22nd Mediterranean Conference of , 16-19 June 2014, pp.164-168.

- Book Chapter
  - M. Pieralisi, V. Di Mattia, V. Petrini, G. Manfredi, A. De Leo, P. Russo, L. Scalise And G. Cerri, *The use of the electromagnetic technology in support to visually impaired runners athletes*, Chapter Book in "Visually Impaired: Assistive Technologies, Challenges And Coping Strategies", 2016 Nova Science Publishers, Inc.

  - G. Cerri, A. De Leo, V. Di Mattia, G. Manfredi, V. Mariani Primiani, V. Petrini, M. Pieralisi, P. Russo, L. Scalise, *Electromagnetic Technologies as Travel Aids for Visually Impaired Subjects*, in B. Andò, F. Siciliano, V. Marletta, A. Monteriù, Ambient Assisted Living (Springer 2015), pp. 159-167

- Patent
  - G. Cerri, A. De Leo, V. Di Mattia, G. Manfredi, V. Petrini, M. Pieralisi, P. Russo, L. Scalise, 2016, *Sistema elettromagnetico per attività fisica autonoma di atleti non vedenti o ipovedenti.*
    IT 102016000009513UB2016A000181, filled January 29, 2016.

1.2. EM contact-less sensors for AAL applications

AAL is a research field of great interest and growing attention. In fact, in the last decade there was an increasing demand for unobtrusive/contact-less solutions for monitoring the indoor living environment and also able to satisfy the request of the aging population. Real-time monitoring of physiological signals such as breathing rate, heart rate, temperature and blood pressure are considered emergency indicators and important predictive parameters for many pathologies. In general, the traditional procedures to gather vital signs from human body require the use of one or more electrodes, cables and chest belts to be applied to the patient, causing him discomfort and stress. On the other hand, a remote monitoring ensures the subject's comfort and, most importantly, it reduces the intervention of medical personnel and of subject cooperation. A suitable solution for the non-contact monitoring is represented by the use of EM sensing. In this context, a novel EM device was realised, based on the transmission of a frequency sweep signal, from 1 to 6GHz, which allows to detect the respiration rate, analysing the variation of phase of the reflection coefficient S_{11}, due to the movements of thorax. The proposed EM system is also able to record long-time sleep breathing activity, highlighting the presence of apnea events. In the end, it is investigating on the possibility to detect the heart rate with the same approach, analysing the relation between the heart movement and the EM signal reflected by the human chest.

My contribution concerned about:

- the investigation of the allowable distances between the target and the antenna for the proper detection of the breathing and heart rate;
- data processing;
- the script development in MATLAB for the detection of the target position.

The following publications describe in details what has just been presented above:

- Conference Proceeding
  - V. Petrini, V. Di Mattia, G. Manfredi, A. De Leo, P. Russo, L. Scalise, G. Cerri, *An Electromagnetic Contact-less System for Apnea Monitoring*, 2016 IEEE Smart Cities, 12-15 Sept. 2016, Trento (Italy).

  - L. Scalise, V. Petrini, V. Di Mattia, P. Russo, A. De Leo, G. Manfredi and G. Cerri, *Multiparameter Electromagnetic Sensor for AAL Indoor Measurement of the Respiration Rate and Position of a Subject*, in Instrumentation and Measurement Technology Conference (I2MTC), 2015 IEEE International, 11-14 May 2015, pp.664-669.

  - P. Russo, V. Petrini, L. Scalise, V. Di Mattia, A. De Leo, G. Manfredi and G. Cerri, *Remote monitoring of breathing activity and position of a subject in indoor environment: the HDOMO 2.0 project*, Proceedings del 6° Forum Italiano dell'Ambient Assisted Living (forITAAL2015), 19-22 May 2015, Lecco, pp 136-145.

  - V. Petrini, V. Di Mattia, A. De Leo, P. Russo, V. Mariani Primiani, G. Manfredi, G. Cerri, L. Scalise, *Ambient assisted living electromagnetic sensor for continuous breathing monitoring applied to movement analysis: a preliminary study*, Mechatronic and Embedded Systems and Applications (MESA), 2014 IEEE/ASME 10th International Conference on, 10-12 Sept. 2014, pp.1,5.

  - V. Di Mattia, V. Petrini, E. Pallotta, A. De Leo, M. Pieralisi, G. Manfredi, P. Russo, V. Mariani Primiani, G. Cerri, L. Scalise, *Design and realisation of a wideband antenna for non-contact respiration monitoring in AAL application*, Mechatronic and Embedded Systems and Applications (MESA), 2014 IEEE/ASME 10th International Conference on, 10-12 Sept. 2014, pp.1,4.

- Book Chapter
  - V. Di Mattia, G. Manfredi, M. Baldini, V. Petrini, L. Scalise, P. Russo, A. De Leo, G. Cerri, *Theoretical Model for Remote Heartbeat Detection Using Radio-frequency Waves*, Proceedings del 7° Forum Italiano dell'Ambient Assisted Living (forITAAL2016), 22-23 June 2016, Pisa (Italy), in press on Lecture Notes in Electrical Engineering, Springer.

  - V. Petrini, V. Di Mattia, A. De Leo, P. Russo, V. Mariani Primiani, G. Manfredi, G. Cerri, L. Scalise, *Domestic monitoring of respiration and movement by an electromagnetic sensor*, in Andò B., Siciliano F., Marletta V., Monteriù A., Ambient Assisted Living (Springer 2015), pp. 133-142.

1.3. Analytical model to characterise the diffracted field by a human body

The proper design and development of the EM systems needs a good understanding of the signal propagation in the environment around a human body and of the interaction between the body and the the field radiated by antenna, also considering its characteristics. Usually these preliminary studies are carried out through several simulations, facing with the complexity and massive memory involved in the detailed modelling of the human body. So the last three years were dedicated to the development of an analytical model, able to characterise the reflected fields by a monitored target for AAL applications. The features were to be the accuracy and in the meantime the reduction of the computational burden to avoid the problems suffered by the numerical tools. This work will be the topic of this thesis and deepened in the following chapters. The presentation of the assumptions on which is based the model, and its applications are described in the following papers:

- Journal
  - G. Manfredi, V. Petrini, V. Di Mattia, A. De Leo, P. Russo, L. Scalise And G. Cerri, *A 3-D Human Body Model for the Movement Detection in Ambient Assisted Living Applications*, IEEE Transactions on Magnetics, 2016, **under review**.

  - G. Manfredi, V. Petrini, V. Di Mattia, A. De Leo, P. Russo, L. Scalise And G. Cerri, *Development of an analytical electromagnetic model based on PO approach, to characterise the field diffracted by a human body*, IEEE Antennas and Propagation Magazine, 2016, **under review**.

- Conference Proceeding
  - G. Manfredi, V. Petrini, V. Di Mattia, M. Pieralisi, A. De Leo, P. Russo, L. Scalise And G. Cerri, *A 3-D body model for physical activity monitoring by microwave radiation*, Microwave Symposium (MMS), 2015 IEEE 15th Mediterranean, Lecce, 2015, pp. 1-4.

Chapter 2.

Introduction

In almost every country, the proportion of people aged over 60 is growing faster than any other age group. Although population aging is the results of a long period of good health and a sustained sense of well-being, it could be associated with more illness and disability [1]. Most of the existing health systems are at limit of their resources and do not possess the capacity or framework to face the increasing needs of an aging population [2]. This highlights the importance of monitoring individuals in their homes and implementing preventive strategies in order to predict many diseases. Respiratory rhythm (RR), heart rate, blood pressure and body temperature represent the full set of vital signs whose daily monitoring may be tools for the prevention and early diagnosis of adult diseases. As an instance, a sudden RR change is one of the strongest predictors of mortality [3, 4]. Many studies have shown that an abnormal RR can predict it up to 72 hours prior to the arrest [5]. Moreover, RR as well as heart rate monitoring allow the diagnosis of many cardiovascular diseases [6], such as hypertension, atherosclerosis, stroke, heart failure [7], cardiac arrhythmias, and sudden death [8], or of important breathing disorders such as bronchitis, asthma and sleep apnoea.

Despite these evidences, two studies found out that in general the level of documentation of vital signs in many hospitals is extremely poor [9, 10] and in particular the RR is often not recorded, even when the patient's underlying condition constitutes a primary respiratory problem. As a matter of fact, RR as well as sleep apnoea monitoring are often neglected mainly due to shortcomings of the measurement techniques [11], which usually cause discomfort and stress (see Figure (2.1)). Some examples are: spirometry, nasal thermocouples, respiratory belt transducers, inductance pneumography, pneumatic respiration transducers, whole-body plethysmography [12], and others [13–17].

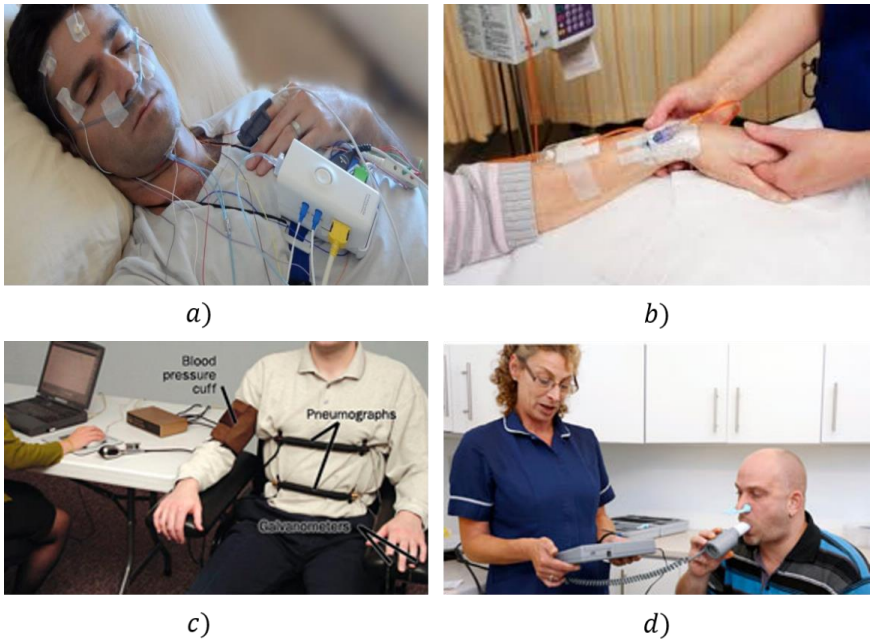

Figure 2.1.: Traditional procedures to gather vital signs: a) electrodes, b) cannulas, c) inductance pneumography, d) spirometry

[1] All these methods may bring discomfort and inconvenience to the subject and medical personnel because they don't include a system that enables the constant measuring of the main vital signs, they don't take measurements in real time in a comfortable manner, or are expensive and not affordable for local hospitals [18]. For example the apnoea monitor, that uses impedance pneumography [19], is attached to the patient using appropriate sensors for the measurement techniques, with evident issues in terms of comfort and repeated failures due to artifact movements: mattress motion sensors, pneumatic abdominal sensors, carbon dioxide (CO2) sensors, cannula, etc.

These issues have achieved a growing demand for *unobtrusive/contact-less*

[1]Figure 2.1/a) is taken from the website *SIAsT - Servizio Infermieristico Assistenziale Territoriale/Polisonnografia* - `http://www.siast.it/servizi-e-prestazioni/esami-strumentali/`;
Figure 2.1/b) is taken from the website *1000 livesplus - Improving care through reducing use of cannulas and catheters* - `http://www.1000livesplus.wales.nhs.uk/stop-psc`
Figure 2.1/c) is taken from the website *When a polygraph test is judged inconclusive-TCS open seesame-solved* - `http://piyadasa15.blogspot.it/2012_08_01_archive.html`
Figure 2.1/d) is taken from the website *NHS - Spirometry* - `http://www.nhs.uk/Conditions/spirometry/Pages/Introduction.aspx`

monitoring solutions of vital signs in order to improve patients' quality of life, reducing hospital stays and, consequently, medical costs. Moreover, in the context of AAL, the monitoring with contact-less and remote techniques of patients, who live at their homes and therefore out of specialised environments, not only increase subject's comfort and avoid privacy issues but also reduce the level of collaboration required from the subjects, which represents a key point when the targets are senior people. Recently, some non-contact solutions have been proposed in literature, for example based on imaging sensors, such as normal webcams [20], infrared thermography [21], or on EM systems. The use of EM sensing allows to monitor the respiration activity of a target with non-contact measurements at significant distances (a few meters). This aspect may represent a clear advantage because an EM system may be easily installed inside hospital rooms or even at home, without the need of a direct view of the target, nor the intervention of medical personnel or subject cooperation. Moreover, the EM monitoring can be applied to dressed people or patients in bed under blankets, without the discomfort of contact sensors nor privacy issues typical of optical systems. The EM systems proposed in literature are mainly based on the use of Continuous Wave (CW) microwave reflectometric radar [22], Ultra Wide Band (UWB) [23,24] techniques or intermediate solution between CW and UWB approaches, joining the advantages of both [25–27]:

- They are simple to realise and don't interfere with other existing systems (*features of CW technology*).
- They are characterised by low transmitting power to the benefit of lower energy consumption and by high speed data transfer over very short distances at low power (*features of UWB technology*).

In the meanwhile there is an increasing development of completely unobtrusive sensors, woven into wearable objects, where the information, collected into smart garments, can be transmitted over some distance and further analysed. These technologies enable the people to carry their personal body area network making patients wireless within the hospital, especially, in intensive care units and operating theatres. This not only enhances patient comfort, but it also makes the work of doctors and nurses a lot more efficient and easy. Hence Wireless body area network (WBAN) [28–30] represents a new enabling system that has promising potential for health monitoring applications. A WBAN consists of several wearable sensors placed in close proximity to a human body, using the body as a conduct for data transmission. It has the potential to continuously and remotely monitor and log a patient's vital physiological parameters, without significantly obstructing the patient's normal daily activities. The collected physiological parameters are transmitted wireless to a receiver to which medical professionals can easily access, so that they can perform neces-

sary actions [30].

The proper design of a contact-less sensors as well as the development of an accurate WBAN require the studies of the interaction mechanism between the EM waves and the body. The propagation mechanism of the wireless radio waves on/inside the body [31], the on-body channel characterisation [32] or the analysis of scattering parameters near to a monitored subject [33, 34] are usually studied by means of measurements or several simulations. The understanding of the signal propagation around the body is essential but not devoid of problems: the measurements are time consuming, as well as the numerical tools, that required in addition a huge computational burden.

In the Antenna Laboratory of the Department of Information Engineering at UNIVPM, the main activities focus on realisation of EM systems, addressed to the remote monitoring of physiological and physical activities of a subject for AAL applications, whose proper design is preceded by several tests and simulations. The following section will be dedicated on the description of the numerical tool *CST MICROWAVE STUDIO (CST MWS)* adopted by our research group, highlighting advantages and disadvantages of the used domain solvers and the main problems occuring to carry out the analysis mentioned above.

2.1. EM methods used in CST MICROWAVE STUDIO

CST MWS is an EM commercial tool based on EM methods that provide solutions to the Maxwell's equations in both time (*Finite Difference Time Domain (FDTD)*) and frequency (*Method of Moments (MoM)*) domains thanks to the different solvers implemented on it [35].

FDTD: Finite Difference Time Domain
The *FDTD* method is a direct solution to Maxwell's time-dependent curl equations and solves the problem in time-domain. It allows to analyse the effects of reflection and radiation and also to model the wave propagation in complex media such as anisotropic, lossy, time-varying and nonlinear media. *FDTD* method is one the most powerful methods in solving problems involving EM wave interactions [36].

Advantages: *FDTD* method is one of the most frequently used methods, thanks to its versatility and the ability to handle complex structures. In addition, the main reason for using the *FDTD* approach is the excellent scaling performance of the method as the problem size grows [37].

Disadvantages: *FDTD* is a computationally intensive method and for high accuracy requires too computer memory resources and considerable calculation time.

MoM: Method of Moments
The *MoM* [38] is a full wave solution of Maxwell's integral equations in the frequency domain and it is classified as a low frequency method used to solve volume integral equations and surface scattering problems in the frequency domain. Because the electromagnetic sources are the quantities of interest, the *MoM* is very useful in solving radiation and scattering problems.

Advantages: *MoM* is significantly more efficient in terms of computational resources for problems with a small surface/volume ratio. Moreover, further advantage of the *MoM* is that it is a *source method* meaning that only the structure in question is discretized (not the whole free space) and consequently, the propagation distance does not degrade the accuracy of the results.

Disadvantages: Full-wave techniques such as *MoM* generally suffer from poor scalability. This limits the electrical size of the problems that can

be solved on typical computers. Conceptually, it works by constructing a *mesh* over the modelled surface, nevertheless for many problems, *MoM* is significantly less efficient than volume-discretization methods (*Finite Element Method, Finite Difference Method*). Additionally, the boundary element formulations typically give rise to fully populated matrices, with the consequent growth of the storage requirements and computational time, proportional to the square of the problem size (N^2).

Table 2.1.: Summary table of advantages and disadvantages of the EM methods

EM methods	*Advantages*	*Disadvantages*
FDTD	• Versatility and the ability to handle complex structures; • Excellent scaling performance as the problem size grows.	• Computers resources and time consuming method.
MoM	• Efficient for problem with a small surface/volume ratio; • Only the structure in question is discretized (not the whole free space).	• Poor scalability; • Memory consumption; • Increasing time computation.

As it has been highlighted in the section (2), the proper design of the EM sensors, addressed to the remote monitoring of the vital signs of a subject, must be preceded by the study of the propagation mechanism of the electromagnetic waves and of their interaction with the body. It follows that the environment to be analysed is mainly made up by:

- human body whose dimensions are on average 170cm X 60cm X 30cm [39];
- antenna whose dimensions and typology depend by the choosen frequencies (from 2GHz to 10GHz) and the application to which is addressed;
- space whose dimensions strongly depend by the adopted distances between the antenna and the observed subject (from 4m to 10m).

Due to the poor scalability of *MoM*, it proves to be less efficient than *FDTD* which is consequently used by our comunity for these kind of analyses. The

FDTD method allows to handle complex structures but requires huge resources and computational time. An example is reported below.

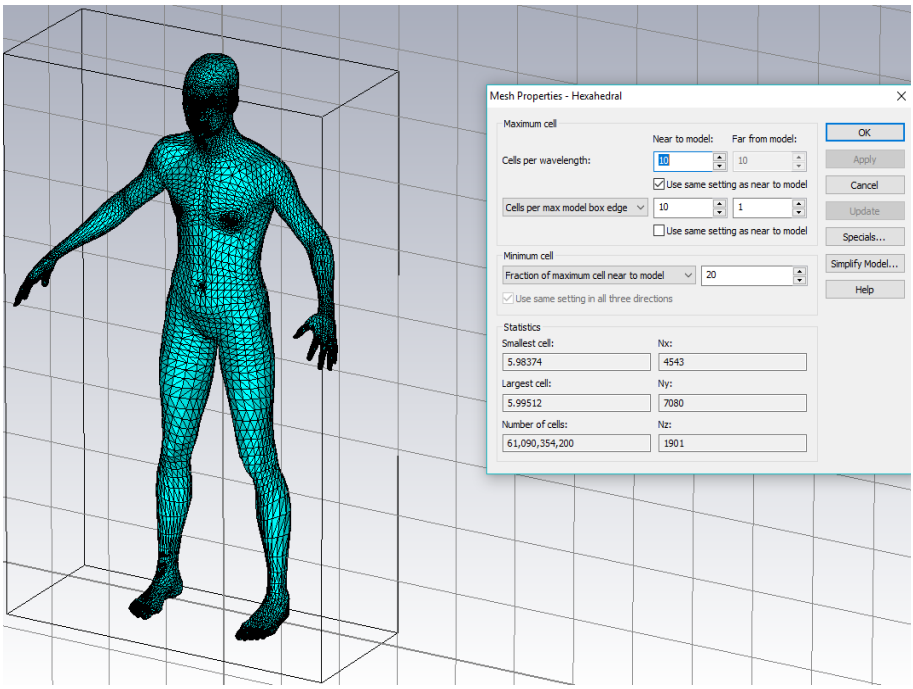

Figure 2.2.: Human body made by *MakeHuman* software and imported in CST MWS

A human body was made by means of *MakeHuman* software [40], whose dimensions 170cm X 60cm X 30cm were selected in accordance with those of a realistic body [39]. The work frequencies 2-6GHz were choosen because they are the most proper frequencies for a real-time monitoring of breathing rate or body activities as pointed out by the recent works [25, 26]. The body was imported in CST MWS tool and discretised by hexahedral meshes, picking 10 cells for wavelength. The accuracy of the simulation strongly depends on the selected numbers of cells for wavelength; 10 is the minimum numbers of cells which must be selected to consider the computational error negligible (See *Appendix* (B)). It follows that the total number of cells is more than 61 billion, as shown in Fig. (2.2), whose simulation requires a computational burden that clearly cannot be affordable by normal calculators. Usually the parallel computing of more than two cluster nodes is used to optimize the computing performances [41].

A further problems is represented by the computational time required by the quoted simulations which varies from the 4h if several cluster computers are adopted in parallel, to more than 17h if a single calculator is used, as it will be highlighted in detail in the chapter (3).

In view of the issues occuring in the numerical calculations, the aim of the research was the development of an EM model which allows the study of the interaction between the EM waves and the body, avoiding the problem of the computational burden. In the following section the proposed model and the topics deepened in each chapters will be presented.

2.2. Aim of Ph.D thesis

The purpose of the thesis is to develop an EM model which allows to analyse how some parameters such as work frequencies, distance, number and/or dimensions of the antennas and kind of movements and dimensions of a target, affect the fields scattered by a monitored subject, features useful for the proper design of the EM sensors. For this reason the aim of Ph.D. research was the development of EM model based on *Physical optics (PO)* approach able to characterise the diffracted field by a human body.

PO: Physical Optics
PO [42] is a method for approximating the high frequency surface currents, allowing a boundary integration to be performed to obtain the fields. *PO* is an intermediate method between full wave electromagnetism, which is an exact theory, and *geometric optics (GO)*, which is a ray-based technique that models objects based on optical propagation, reflection and refraction theory [43, 44].

Advantages: PO models the interference and the polarisation effects for which the ray approximation of geometric optics is not valid.

Disadvantages: PO requires an additional method to compute the contribution due to the diffraction phenomena such as the PTD (*Physical Theory of Diffraction* [45]) which is applied jointly to the PO formulation [46].

Table 2.2.: Summary table of advantages and disadvantages of the PO

EM methods	*Advantages*	*Disadvantages*
PO	• It models the interference and the polarisation effects.	• It doesn't take into account the fields diffracted by the edges; • Run-time grows exponentially with multiple reflections.

A EM model based on *PO* allows to calculate the reflected fields in everwhere only determining the surface equivalent current densities flowing on the surface of the target without the discretisation and the calculation of the total observed space as required by the *FDTD* method. Consequently, the analytical model ptoves to be efficient, light from the point of the computational burden and sufficiently accurate, avoiding the problems of memory consumption and of huge time computation, typical of most of the EM methods explained in the section (2.1). The work will be deepened in this thesis as follows:
In **Chapter** (3) several preliminary studies will be discussed for the choice of a suitable human model with a particular regard on the validity of the use of homogeneous canonical shapes to model the body parts. Moreover, a comparison between simulations and measurements of a moving target has been carried out to test the feasibility of the adopted choices.
In **Chapter** (4) the proposed analytical model will be described together with the definition of the human body model and of the analysed scenario's geometry.
In **Chapter** (5) several tests regarding static targets, carried out to evaluate the accuracy and the feasibility of the model, will be presented and commented.
The **Chapter** (6) is dedicated to the radar Doppler techniques implemented in the model to analyse and discriminate general activities of a monitored target.
The **Chapter** (7) outlines the conclusions and discusses some other possible applications of my EM model.

Chapter 3.

Preliminary Studies

The proper design of an EM sensor, for several biomedical applications or for remote monitoring of physiological signals, involves the study of the propagation mechanisms of the EM waves on and inside the body, with the consequent need for a human model. The coupling effects of the human body on antennas are usually studied by means of experimental investigations or computer simulations, using general purpose EM simulators and, in order to quantitatively analyse the interaction, the evaluation by use of several phantoms is widely performed. Some of the major challenges to face are the manufacturing of the phantoms and, the complexity and massive memory involved in the detailed modelling of the human body in the numerical tools.

Empirical studies are often made with a Specific Anthropomorphic Mannequin (SAM). It is a human body phantom [47–49], filled with a homogenous tissue liquid, whose shape, properties and general dimensions are similar to an average human body. Those phantoms are expensive and difficult to use in laboratory, due to the filling with a special liquid of precisely controlled dielectric properties [30, 50].

In many contemporary EM CAD packages, heterogeneous models are available [35, 51–54], representing the inner structure of the human body. In addition, the modelling of the phantoms requires a great amount of computer resources as the discretisation of the model has to be accurate to represent details of inner organs. Most of the EM simulators indeed perform an automatic meshing on the simulated objects using an arbitrary number of cells per wavelength. If a large number of cells per wavelength are selected, the total number of cells will be very large. On the other hand, if a small number of cells per wavelength are selected, the accuracy of the simulation will be very poor (This issue will be deepened in the section (3.2)). As a consequence, in order to overcome this problem, usually only a small part of the human body is usually simulated, such as head or neck in dosimetry studies or torso or single arm to design a proper WBAN [55, 56].

Given these issues, several preliminary studies were carried out to choose the suitable human model which represents the best trade-off between accuracy and computational efficiency. These results will be presented and discussed in this chapter with a particular regard on the validity of the use of homogeneous canonical shapes to model the body parts. It will also present the comparison between measurements and simulations of a moving target, to test the feasibility of the adopted choices.

3.1. Canonical shapes to represent the human body parts

The human body has a very complex shape and its representation is a very heavy burden from a computational point of view. However, in many cases a detailed description is not required, such as in the situation where the spectral content of the body movements is under investigation. In fact, recent works [25, 26] have pointed out that the most proper frequency range for a real-time monitoring of breathing rate or body activities is 2-6GHz. In this frequency range, the skin depth δ is shorter than 1.5cm[1]. It follows that, a body representation with an accurate knowledge of internal tissues and organs is computationally expensive and useless for evaluating the scattered field, as only a thin external layer interacts with the EM field.

Another aspect concerns the representation of external details of the body, as nose, mouth, ears, fingers, and so on. The great variability of shape and dimension of these parts of the body from one individual to another makes ineffective a too accurate modelling. Consequently, to evaluate the EM backscattering, head, chest, arms and legs can be modelled with primitive shapes (spheres, cylinders and parallelepipeds). In this way, the approach reduces the computational cost, and at the same time, it allows to generate a structure flexible enough to change posture and position. In order to choose the most suitable simplified model, a commercial full wave EM solver (CST MICROWAVE STUDIO (CST MWS) [35]) was used. The first human part considered was the head, because it is the most complex part of the body, characterised by many anatomical details. Therefore it seems difficult to represent the head with a simple geometrical shape, and for this reason, the case study is suitable to stress the model. The EM field reflected by the human head provided by the SAM phantom was compared to the backscattering of several spheres of different radius with the aim to verify if the anatomical details of head, as nose, mouth, and ears, were significant for the evaluation of the diffracted field.

[1] The dielectric properties of the skin adopted for the calculation of δ are: $\epsilon_r = 42$, $\sigma = 3.6 S/m$ [57]. A definition of the skin depth δ is presented by D. Andreuccetti in *"Dielectric properties of human tissues: definitions, parametric model, computing codes."* [58]

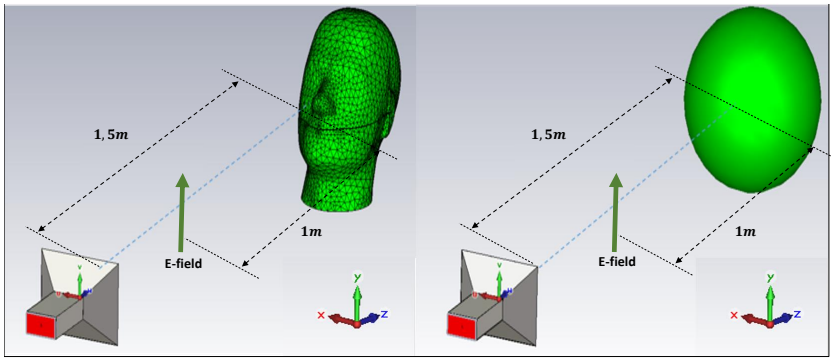

Figure 3.1.: Geometric configurations of the problems implemented in CST MWS to compare the E-field reflected by the SAM phantom head (left) and by the spheres of different radii (right).

Three spheres were taken into consideration: the first has a radius of 108.9mm, in order to have a volume equivalent to the SAM head model. The second one has the radius of 100mm, which corresponds to the radius of longitudinal section of the SAM head model, and the third one, with the radius equal to 109mm, corresponding to the sagittal section (3.1). It was assumed that the spheres and the SAM model are filled with a homogeneous dielectric with the same properties as skin (relative permittivity $\epsilon_r = 42$, and conductivity $\sigma = 3.6 S/m$ [57]). Both were placed at a distance of 1.5m from a horn antenna along z direction (See Fig. (3.1)). The excitation signal is a modulated Gaussian pulse generated by the CST MWS software, whose spectrum is in the range 3-5GHz. The wave travels in free space along the z direction and it is linearly polarised, with the E field parallel to y-axis. Figure (3.2) shows the E field reflected by the three spheres and the SAM phantom head, observed at a distance of 1m along the z-axis.

Table 3.1.: E-field reflected by SAM and the spheres: Simulation setup

Setting	
antenna	horn
frequencies	3-5GHz
distance antenna-target	1.5m
polarization	v-pole
field intensity	1V/m (default)
calculation time	$\approx 8h$

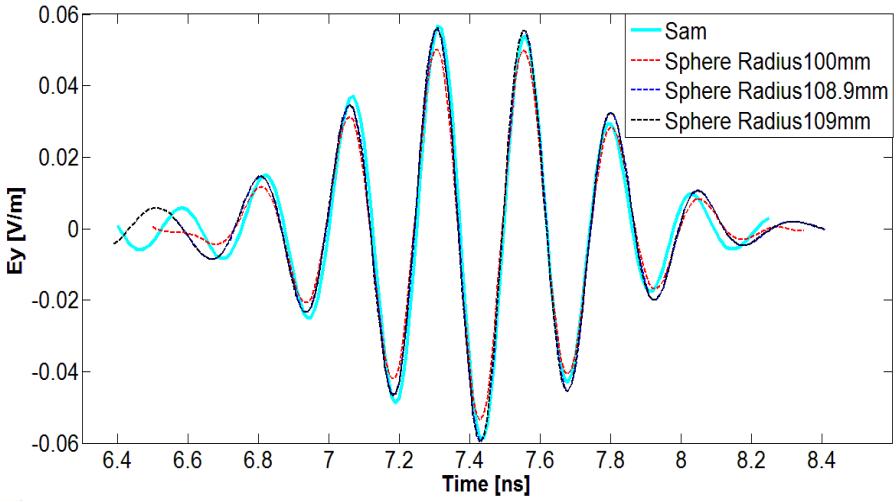

Figure 3.2.: Comparison of electric field backscattered by the SAM head and three spheres, observed at a distance of 1m along the z-axis

For a better comparison among field time histories, the cross-correlation was evaluated [59]:

$$(f \star g)[n] \stackrel{\text{def}}{=} \sum_{m=-\infty}^{\infty} f^*[m]g[m+n]. \tag{3.1}$$

being f and g the discrete functions, representing respectively the E fields reflected by SAM and the three spheres, n the displacement also known as *lag*, and f^* the complex coniugate of f. The function was implemented in MATLAB [60] by the function $xcorr$[2], through which was calculated the similiarity of the observed reflected waves. Table (3.2) reports the maximum amplitude of the backscattered electric field and the result of the cross-correlation, calculated between the diffracted field of each sphere and of the SAM model's head.

[2] $r = xcorr(x, y)$ returns the cross-correlation of two discrete-time sequences, x and y. Cross-correlation measures the similarity between x and shifted (*lagged*) copies of y as a function of the lag. If x and y have different lengths, the function appends zeros at the end of the shorter vector so it has the same length, N, as the other (See the website `https://it.mathworks.com/help/signal/ref/xcorr.html`).

Table 3.2.: Maximum field intensity and cross-correlation between the E-field waveforms diffracted by the spheres and the Sam model's head

Target	*E-field [V/m] (max intensity in absolute value)*	*cross-correlation*
Sam	0.0568	1
Sphere - Radius 100mm	0.0503	0.89
Sphere - Radius 108.9mm	0.0560	0.99
Sphere - Radius 109mm	0.0562	0.96

It can be appreciated a good agreement between the sphere with 108.9mm radius and the SAM head, both in terms of correlation and in terms of maximum strength. Therefore, the sphere with equivalent volume of the SAM's head provides a response that best fits the realistic situation. Moreover, in order to observe how the distortion of wave depends on the scattering surface, the reflected waves were normalised respect the own maximum peak value and then correlated, applying the equation (3.1), with final result around 0.98, as it depicted in Fig. (3.3).

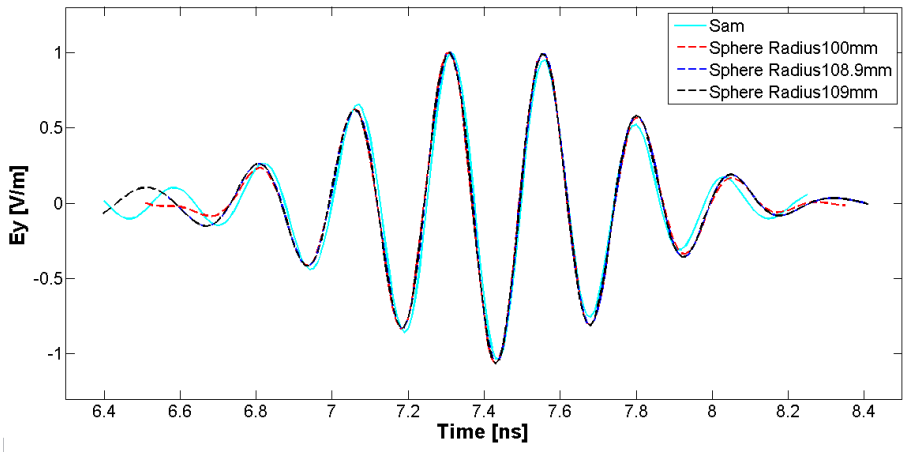

Figure 3.3.: Comparison between normalised re-radiated waves

The same results can be obtained also by replacing the other anatomic parts of the body (*neck, torso, arms and legs*) with elementary geometric shapes such as cylinders and parallelepipeds. It follows that in the range of a few GHz, the representation of anatomic details can be replaced with elementary shapes, without any significant distortion of the backscattered waveform and with a negligible error for what concerns its peak value.

3.2. Analysis of the E-field backscattered by the whole body

The results achieved in section (3.1) were extended to the whole body, and, in particular, it was analysed the possibility to retrieve the field backscattered by the whole body as superposition of the field reflected by separated body parts.

Referring to the model presented in the works [50, 56], the human body was modelled as a collection of spheres, cylinders and parallelepipeds to reproduce head, chest, arms and legs, whose dimensions are in accordance with those of a realistic body [39]. The height of the human model is 1.68m and each part is characterised by dielectric properties of the skin with $\epsilon_r = 42$ and $\sigma = 3.6 S/m$ [57]. Furthermore all the parts of the body were considered disjointed from each other in order to make the structure more flexible and able to be configured in different positions. This choice may affect the equivalent current density distribution but, it was validated by A. De Leo et al. in the work [61], by the comparison between full wave numerical simulations where the elements of the body were reproduced joined and disjoined from each other. The result is depicted in Fig.[3] (3.4)

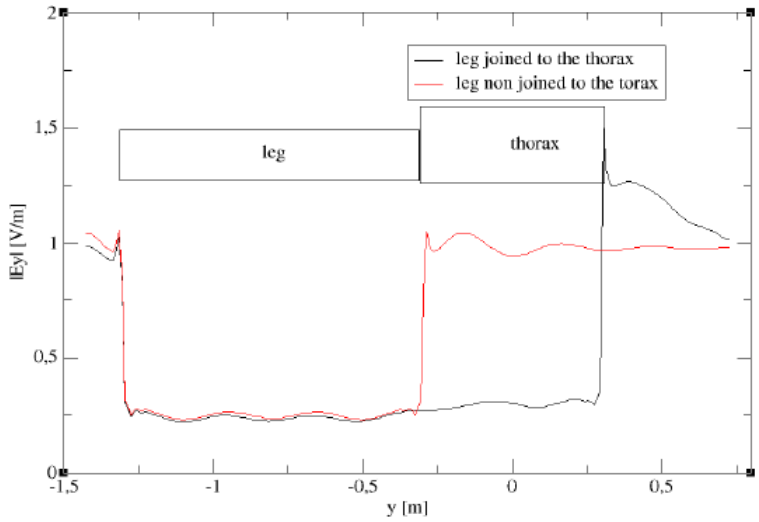

Figure 3.4.: E field distribution inside a leg illuminated at 1 GHz by a plane wave with $|E| = 1 V/m$, considering only the leg (red line) and the whole human body model (black line)

[3] SOURCE: Picture taken from data by A. De Leo et al., "*Breath detection of humans buried in a homogeneous lossy medium: a simplified analytical model*", 2012 International Symposium on Electromagnetic Compatibility (EMC EUROPE), IEEE

Figure (3.4) shown an equivalent distribution of the E-field, observed inside an element either joint or not joint with other body parts, at frequency 1GHz. This because it takes advantage of the relatively high frequencies of the pulse spectrum, corresponding to wavelengths shorter than body parts dimensions, so that the mutual coupling among the body parts can be considered negligible.

Both total body and each of its parts, depicted in Fig. (3.5) were individually simulated to demonstrate that the total field scattered by a human body can be approximated as the sum of the fields reflected by single body parts. The objects were illuminated by a plane wave at frequencies ranging from 3 to 5GHz, corresponding to a modulated Gaussian pulse in time domain. The electromagnetic wave, linearly polarised, travels in free space along z direction, with E field directed along y-axis and a default intensity value of 1V/m.

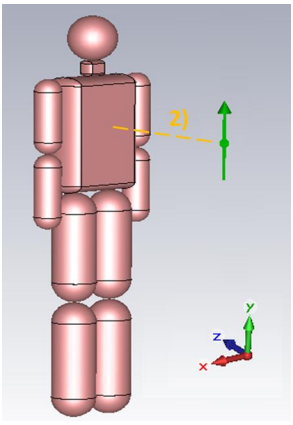

Figure 3.5.: Human body reproduced by primitive shapes implemented in CST MWS)

Table 3.3.: E-field reflected by total body and its parts: Simulation setup

Setting	
antenna	horn
frequencies	3-5GHz
distance antenna-target	2m
polarization	v-pole
field intensity	1V/m (default)
calculation time	$\approx 44h$

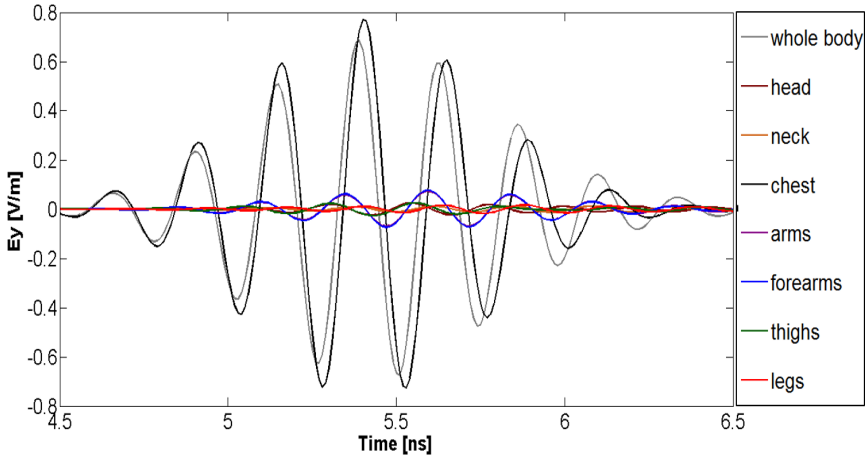

Figure 3.6.: E-fields backscattered by individual elements of the human body and collected at the distance of 1.5m from the antenna (position No 2)

Figure (3.6) reports the E fields scattered by each body parts and collected at the distance of 1.5m away from the antenna in the position No 2. As expected, at this position, the field scattered by the chest is greater than any other E fields, because of its dimension and flat surface.

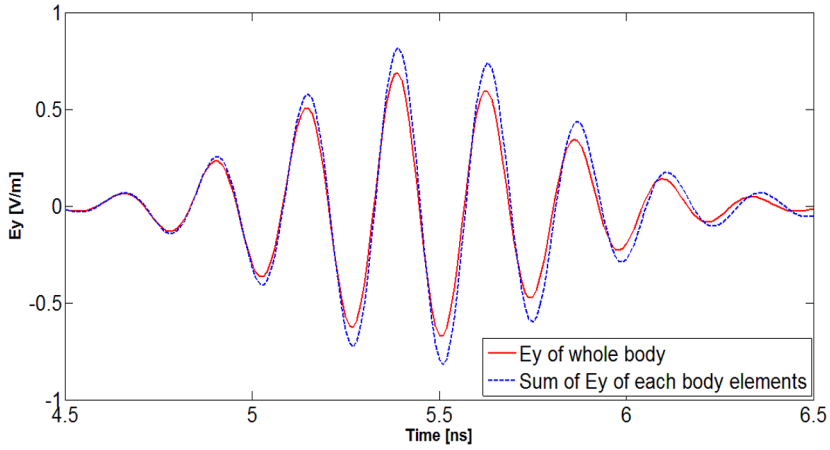

Figure 3.7.: Comparison between the total field scattered by the whole body phantom and the sum of the fields scattered by each body part evaluated in the position No 2

Figure (3.7) shows the comparison between the sum of the fields scattered by the total body and by its individual parts, evaluated in the position No 2. The cross-correlation between these two curves is 0.85. This relatively low value (with respect to those evaluated in section (3.1)) is mainly due to the different peak amplitudes whereas the time waveforms are quite similar. This means that:

- the spectral content of the two curves, that is the quantity to be analysed to get information about possible body movements, is the same;
- the amplitude differences are due to numerical accuracy, and do not affect significantly the assumption of negligible mutual coupling among body parts.

To demonstrate these assessments, a simple numerical test was carried out. As spatial discretisation is a critical parameter in every numerical model, further simulations were performed to evaluate its influence on the results. Table (3.4) lists the different resolutions adopted in terms of wavelength, the average number of cells that discretise the body parts for each selected resolution and the calculation time required to simulate each elements. The last column of the table shows the cross-correlation between the sums of the E-fields scattered by the individual parts and by the whole model at different resolutions.

Table 3.4.: Analysis of the numerical accuracy in relation to the cells per wavelength adopted

Resolution (cells per wavelength)	*Average number of cells for each body element*	*Calculation time*	*Cross-Correlation*
λ /7.5	5800000	4h 23min	0.83
λ /10	133490000	10h	0.85
λ /12	227280000	17h	0.89

Table (3.4) highlights that the correlation monotonically increases up when increasing simulation resolution. Therefore, a higher resolution in terms of wavelength leads to better correlation coefficients. As the only difference between the two curves is in term of peak amplitude, no significant distortion can be appreciated in terms of waveform and consequently of spectral content. This is a key result because, to detect the movements of a target located in front of the EM system, it needs to analyse the spectral content of the backscattered pulse.

3.3. Analysis of human motions: comparison between simulated and measured result

The feasibility of evaluating the whole body scattering by dividing the initial problem in a reduced number of much simpler sub-problems, was further validated considering a moving target. In particular, the harmonic content of the signal backscattered by a human subject, performing a sideward arms movement, was simulated using the approach proposed in the previous section (3.2) and measured in the Antenna laboratory of the department of Information Engineering in Ancona. The laboratory set up consisted of a portable Vectorial Network Analyser (VNA), a laptop and a double ridge horn antenna with an aperture of 14cm X 24cm. The signal radiated had a frequency bandwidth 3-5GHz and a power level of 0dBm. The subject was located at a distance of 2.5m in front of the antenna, placed 1.30m above the ground. The backscattered field was acquired in real time by the VNA at the frequency of 3 samples/s. To the purpose of this comparison, at first the volunteer has been asked

- to stay still (time interval No 1, duration $\approx$ 12s);
- to raise up her arms sideways and return to the rest position (time interval No 2, duration $\approx$ 12s);
- to stay still again until the end of the measurement session (time interval No 3, duration $\approx$ 15s).

Table 3.5.: Analysis of human motions: Measure and Simulation setup

Setting	
antenna	double-ridged horn
frequencies	3-5GHz
distance antenna-target	2.5m
polarization	v-pole
power	0dBm
field intensity	1V/m (default)
frequency sampling	3samples/s
measure time	40s
simulation time	$\approx 25h$

Obviously, despite the real human movement is continuous, it was necessarily simulated as a sequence of frameworks corresponding to a different sidewards arms position (0°, 30°, 60°, 90°, 120°, 150° and 180°). Pictures of the experiment were used to synchronise the virtual movements of the arms with the

measurement scenario, as shown in Fig. (3.8)

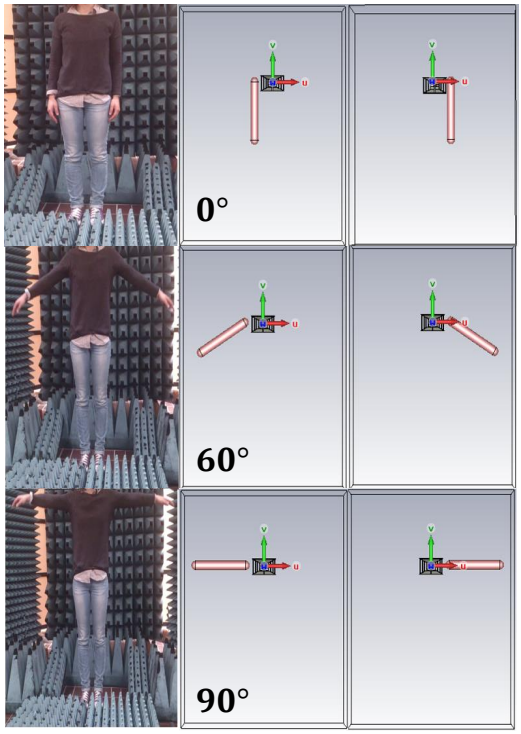

Figure 3.8.: Volunteer with her arms in several positions during the measurement test and the phantom arms configuration used to analyse the same positions with CST MWS

The procedure for the measured and simulated data processing is shown in Fig. (3.9) and explained below:

- **1st STEP:** Measure and simulation of the S_{11}^0 relative the volunteer in still position (See Fig. (3.9) *a)*);

- **2nd STEP:** Measure and simulation of the S_{11}^i relative the volunteer performing the sidewards arms movements (See Fig. (3.9) *b)*);

- **3rd STEP:** Subtraction of the contribution of the static objects to the measured backscattered signal, in order to highlight contribution of moving parts (See Fig. (3.9) *c)*);

- **4th STEP:** Short-Time Fourier Transform (STFT) analysis [25] of the resulting measured and simulated data matrix H (See Fig. (3.9) *d)*). Chosen a moving window, the contribution in magnitude of all transforms for each EM frequency j is considered by taking the sum of the all Fourier Transform

$$M(f) = \sum_{j=1}^{N} | \, STFT_j(f) \, | \tag{3.2}$$

being j the column index of the EM frequencies and f the low frequency at which the body motion is evaluated for spectral density.

The final result is a spectrogram which record the variation of the power spectrum density over time, useful to achieve information about body movements related to any kind of physical activity.

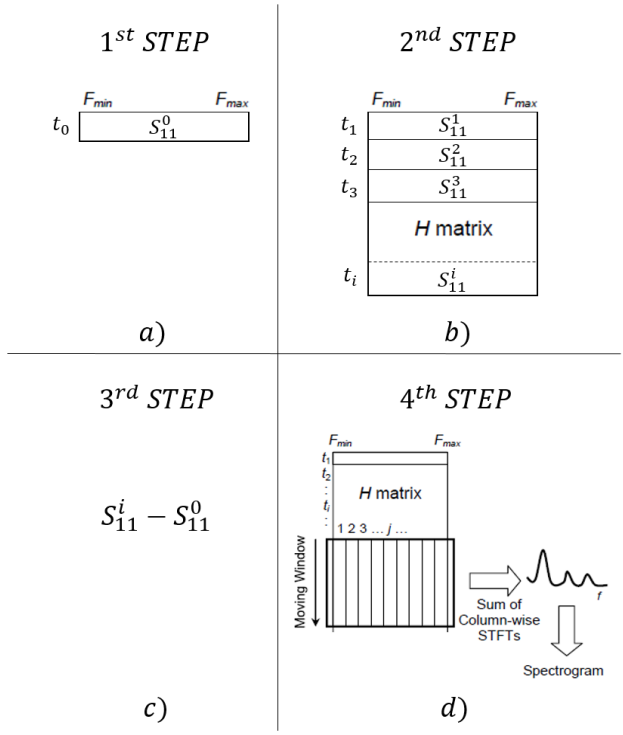

Figure 3.9.: Performed procedure to acquire the measured and simulated spectrogram

Figure (3.10) depicts the spectrogram obtained from the laboratory measurements, where the three time intervals are clearly identifiable. In fact, when the subject is still (0<t<12 s and 24s <t<40s) the power density values are significantly smaller than those obtained in 12s < t <24s, when the subject is moving her arms. More in details, considering the central interval, it is possible to distinguish the harmonic contents relative to the sideward arms movement from bottom to top in the time interval 12-16s, and from top to bottom in the following time interval 20-24s. For both movements the significant harmonic content is between 0.3 and 0.8Hz, represented by the red/orange area.

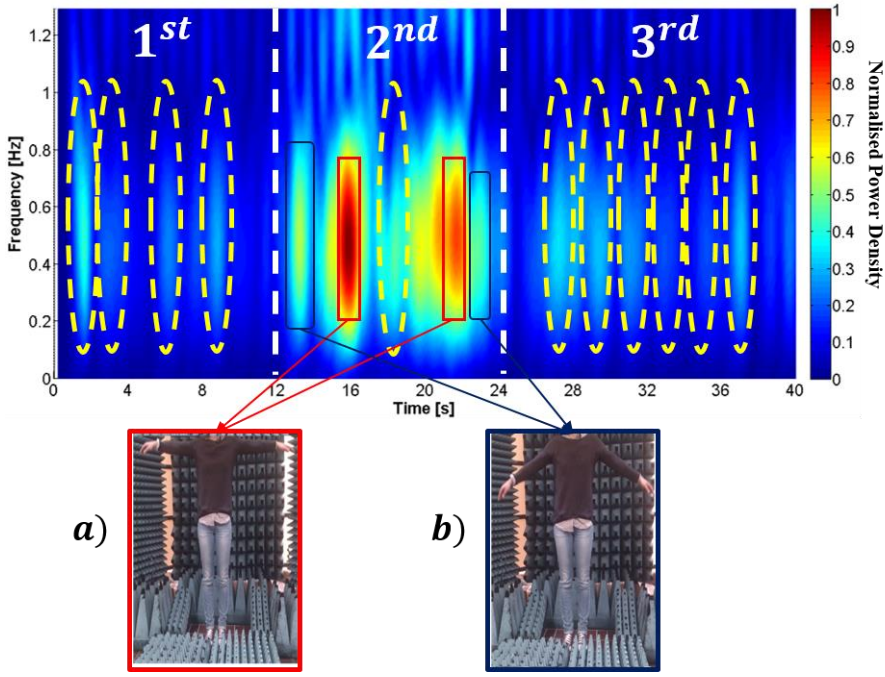

Figure 3.10.: Measured spectrogram relative to the movements of the volunteer. The red/orange areas highlight the sideward arms movement of the subject; the green/white areas represent involuntary movements

Referring to the Fig. (3.10) some evidences can be highlighted:

- Despite in some intervals the volunteer was asked to stay still, some harmonic contents can be visibly observed (yellow circles in Fig. (3.10)). This behaviour could be due to small involuntary movements of the subject (for example backwards and forwards with respect to the antenna)

which modify the phase of the reflection coefficient and consequently the harmonic content of backscattered signals. Moreover, it is worth noting the sensitivity of the system explained in detail in the previous work [25], which is able to detect the breathing activity enhanced by the movement of the chest at this frequency range.

- Two main spectral contributions emerge during the 2nd interval of time. They are in correspondence of arms located at 90° with respect to the body (See Fig. (3.10) *a)*). In this position indeed, the component of speed reaches the maximum value of its harmonic variation. The different power density intensities obtained in correspondence of ascendant and descendent movements (See Fig. (3.10) *b)*) could be explained with the different speed of arms as well as to involuntary small oscillations of the subject.

The simulated spectrogram is represented in the Fig (3.11) The three intervals of time are well outlined once again, the ascendant and descendent arms movements can be distinguished and their significant harmonic content is between 0.3 and 0.7 Hz in good agreement with the measured results.

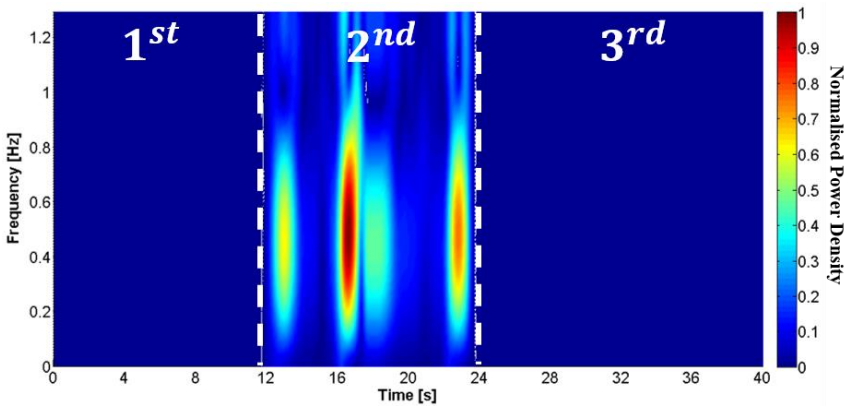

Figure 3.11.: Simulated spectrogram relative to the different sideward arms positions of the human body model proposed

In addition some evidence can be highlighted:

- As expected the harmonic content in the 1st and 3rd interval is null because the simulation does not take into account neither spurious movements nor the respiratory activity that instead are necessarily present in the experiment.

- Accordingly to measured results, two contributions are significantly higher with respect to the others.
- Again, they correspond to arms located at 90° where the component of speed movement reaches its maximum value. In the simulation, the ascendant and descendent movements are equivalent and hence the related power density values are the same. This confirms that the different spectral values measured during ascending and descending phases of the arms are due to the different velocities and spurious movements that in simulation are not taken into account.

These preliminary studies represented a key point for the development of the EM model based on PO approach which will be presented in the following section. The EM model is addressed to the remote monitoring of physical activity of subjects in indoor environments and the analysis deepened in this section gave useful hints for the construction of the human model which made it more efficient than the traditional numerical techniques.

Chapter 4.

Analytical Model Based on PO Approach

In the chapter (2) it has been discussed how the optimal design of Wireless Body Area Networks (WBANs) involves the analysis of interaction between the human body and radio waves. At frequencies in the range of several GHz the human body introduces high radio wave attenuation in the propagation channel. Typically these effects are analysed with computer simulations and experimental investigation [62]. While measurement is a good approach for providing results based on realistic settings, it can be expensive, tedious, and time consuming, especially for development of a propagation channel model that requires a large number of statistical data [31, 63, 64]. Computational approach is well suited for careful study, but it can also be very memory and time intensive, depending on the problem structure and the frequency of interest [30,33,34]. In order to overcome these drawbacks, the purpose of the this Ph.D research was the development and implementation of an analytical EM model that has to be efficient, light from the point of the computational burden and sufficiently accurate to analyse the interactions between the human body and the EM fields.

The aim of this chapter is to present the proposed EM model, based on PO approach to evaluate the fields scattered by the body, first starting from the definition of the human model and of the scenario's geometry.

4.1. Human body model

The proper design of contact-less sensors requires the study of the interaction mechanism between the EM waves and the body, with the consequent need for a human body model. The phantom must be flexible enough to be easily rearranged in order to change quickly posture and position. To this purpose

the following function is chosen

$$f(x,y,z) = \left(\frac{x-x_p}{a}\right)^m + \left(\frac{y-y_p}{b}\right)^n + \left(\frac{z-z_p}{c}\right)^p = 1 \qquad (4.1)$$

In a 3D space the function $f(x,y,z)$ of eq.(4.1) represents the surface of a "cuboid" where x_p, y_p, z_p are the coordinates of the solid's baricenter, a, b, c are the semi-length, the semi-width and the semi-height respectively of the solid and m, n, p are coefficients which define the curvature of the surface for each axis. By means of the proper choice of the parameters a, b, c, m, n, p, a human model was modelled as having 13 body parts (Fig.(4.1)) reproduced by the combination of the canonical geometries of sphere, cylinder and parallelepiped, whose sizes are equivalent to the average human body sizes [39].

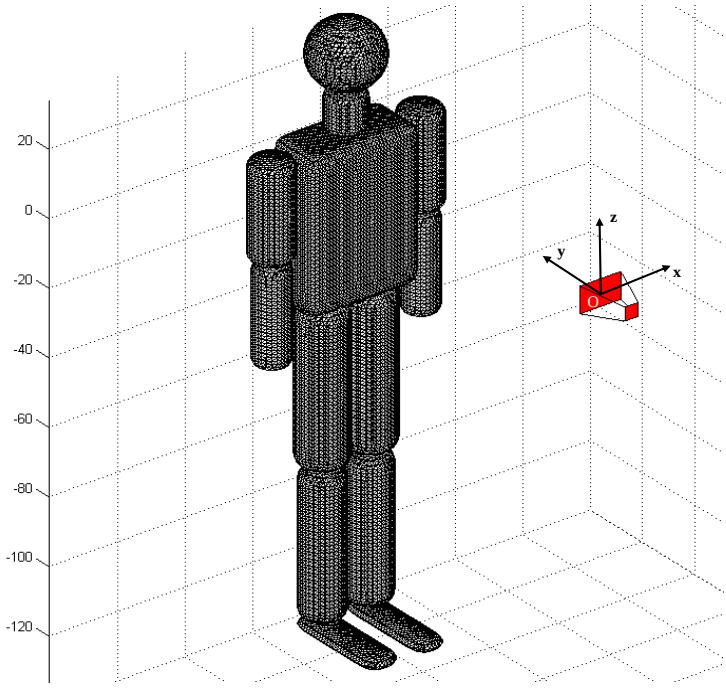

Figure 4.1.: Human model with 13 body parts analytically expressed and implemented in MATLAB

Table 4.1.: Human model parameters

Human element	*Semi-axis*			*Coefficients*			*Shape*
	a (cm)	b (cm)	c (cm)	m	n	p	
Head (H)	10	10	10	2	2	2	Sphere
Neck (H)	5.5	5.5	6	2	2	10	Cylinder
Torso (T)	16	8	23	15	15	15	Parallelepiped
Upper Arm (UA)	6	6	15	2	2	20	Cylinder
Lower Arm (LA)	5	5	15	2	2	20	Cylinder
Upper Leg (UL)	7	7	24	2	2	20	Cylinder
Lower Leg (LL)	6	6	22	2	2	20	Cylinder
Feet (F)	4.5	15.5	2	2	2	10	Cylinder

4.2. Reference system

An important capability of the analytical model is to easily allow for position and orientation change in order to simulate movements and variations of body postures. Hence the choice of the reference system is of paramount importance as it provides the required flexibility to the algorithm for moving bodies but it also greatly affects the EM problem complexity.

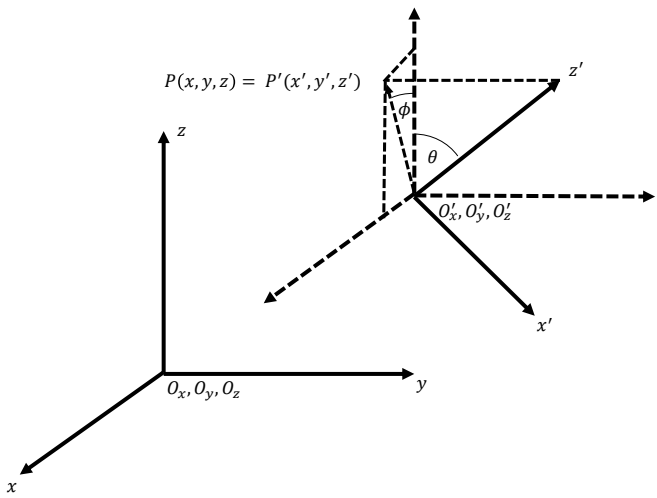

Figure 4.2.: Fixed and mobile reference systems

Referring to Fig.(4.2), (O,x,y,z) is considered as the fixed (or antenna) Cartesian system, whereas (O',x',y',z') is the mobile system (or human body). The

relationship between the coordinates of a point P is:

$$\begin{bmatrix} x \\ y \\ z \end{bmatrix} = \mathbf{R} \begin{bmatrix} x' \\ y' \\ z' \end{bmatrix} + \begin{bmatrix} O'_x \\ O'_y \\ O'_z \end{bmatrix} \tag{4.2}$$

where $\mathbf{R}$ is the rotation matrix, whose columns represent the unit vectors (x',y',z') and the coordinates of the origin (O'_x,O'_y,O'_z) respectively of the mobile system expressed in the fixed system (the choice of a not traditional reference system is due to graphics constrains faced in Matlab software. The reference system adopted in the model is presented in the *Appendix*(A)).

$$\mathbf{R} = \begin{bmatrix} \sin\theta\sin\phi & \cos\theta\sin\phi & \cos\phi \\ \cos\theta & -\sin\theta & 0 \\ \sin\theta\cos\phi & \cos\theta\cos\phi & -\sin\phi \end{bmatrix} \tag{4.3}$$

It is evident that the different choices for θ, ϕ, O' of different cuboids, that simulate the different parts of the body, provide change of the posture. Considering $\theta(t)$, $\phi(t)$, $O'(t)$ as a function of time, animations can be performed.

4.3. Definition of the system's geometry

The proposed EM model is based on the PO approximation which consists of using ray optics to estimate the incident electric field on a surface and, after evaluating a proper equivalent current distribution on the surface, the scattered field is calculated [65–67]. In order to represent an arbitrary incident field E^i, the geometry of the scenario involved in the interaction between the body and the wavefront is firstly defined.

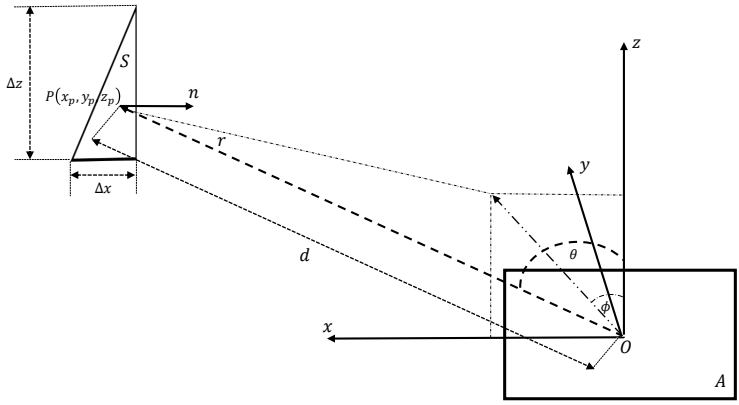

Figure 4.3.: Geometry representation of the interaction between the body surface and the antenna

Figure (4.3) depicts the antenna (A) represented by an equivalent ideal aperture antenna, the fixed Cartesian system (O,x,y,z), centred on the aperture, and the scattering surface element (S), representing a sub area of the radiated body. The angles θ and ϕ define the direction of the vector r which impinges in the point $p(x_p, y_p, z_p)$ of the surface S at the distance d. It is important to highlight that the incident electric field, explained in details in the section(4.4), is calculated in far field condition (although this hypothesis is not essential for the validity of the approach). When the source is in the far field zone, a quasi plane-wave approximation for the EM field impinging on each sub-area of the body surface can be adopted [66]. When the scattered field is considered, the body is the source and the field point is the antenna position. The *Far-field (Fraunhofer) region* [68] is commonly defined for distances greater than $2D^2/\lambda$, λ being the wavelength and D the maximum overall dimension. It is clear that, referring to the average dimension of the whole body, approximately 1,70m [39] and to the working frequencies of the sensors discussed in the chapter(2), the

far field region would be identified from distances greater than 120m. The analytical EM model has the aim to reproduce the real scenario of the contact-less monitoring of a subject in indoor environment where the distances involved are not greater than 10m. As a consequence the whole human body surface is discretised in several sub triangular areas, representing each of them an elementary source for the scattered field. Their dimensions (Δx,Δz) are chosen so that the antenna can be considered in the far field zone for the minimum distance d (Fig.(4.3)) between the antenna and the body, allowing to express the incident field analytically, after assuming a know field distribution on the antenna aperture. However also this hypothesis is not essential for the validity of the approach. The interaction among the fields of adjacent subareas is assumed to be negligible and the sizes (Δx,Δz) are chosen such that the surface S is small enough to consider the currents uniform throughout (*Appendix*(B)). Accordingly, each sub area is identified by a single point $P(x_p,y_p,z_p)$, assuming E^i constant over the whole subsurface. For each point are defined the unit vector of the field point $\hat{r}$ of the field and the unit vector $\hat{n}$ normal to the surface S, according to the following equations:

$$\begin{aligned}\hat{r} &= \frac{x_p}{|\vec{r}|}\hat{x} + \frac{y_p}{|\vec{r}|}\hat{y} + \frac{z_p}{|\vec{r}|}\hat{z} \\ &= l\hat{x} + m\hat{y} + n\hat{z} \qquad (4.4)\\ \hat{n} &= \frac{\nabla f(x,y,z)}{|\nabla f(x,y,z)|} \\ &= l'\hat{x} + m'\hat{y} + p'\hat{z} \qquad (4.5)\end{aligned}$$

where *f(x,y,z)* is given by the eq. (4.1).
The plane containing the unit vectors $\hat{r}$ and $\hat{n}$ and the origin O is the incidence plane *I*. Its equation is:

$$\mathbf{I_x}x + \mathbf{I_y}y + \mathbf{I_z}z = 0 \qquad (4.6)$$

$$\mathbf{I_x} = \begin{bmatrix} m & n \\ m' & n' \end{bmatrix} \mathbf{I_y} = \begin{bmatrix} l & n \\ l' & n' \end{bmatrix} \mathbf{I_z} = \begin{bmatrix} l & m \\ l' & m' \end{bmatrix} \qquad (4.7)$$

In the incidence plane are defined the unit vector $\hat{\mathbf{v}}_\perp$ perpendicular to the plane I and the unit vector $\hat{\boldsymbol{\tau}}$ tangential to the surface S and orthogonal to I, according the following equations:

$$\hat{v}_\perp = \frac{\mathbf{I_x}\hat{x} + \mathbf{I_y}\hat{y} + \mathbf{I_z}\hat{z}}{\sqrt{\mathbf{I_x}^2 + \mathbf{I_y}^2 + \mathbf{I_z}^2}} = v_{\perp_x}\hat{x} + v_{\perp_y}\hat{y} + v_{\perp_z}\hat{z} \qquad (4.8)$$

$$\hat{\tau} = \hat{\mathbf{n}} \text{ x } \hat{v}_\perp \qquad (4.9)$$

4.4. Incident field

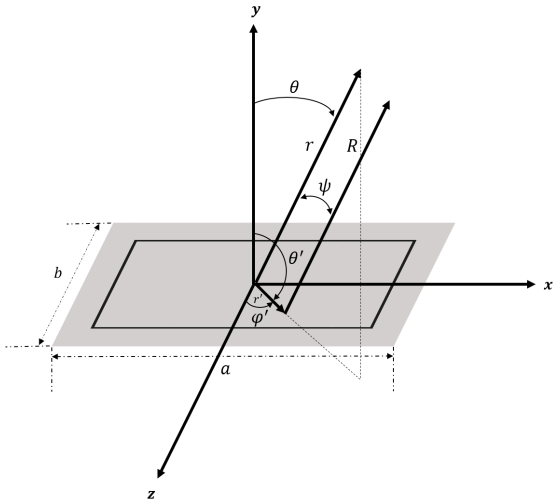

Figure 4.4.: Rectangular aperture on an infinite electric ground plane (*the choice of a not traditional reference system is due to graphics constrains faced in Matlab software)*

The condition that the body is in the far field of the antenna allows us to express the incident field analytically, after assuming a suitable field distribution E_a on the antenna aperture [68]:

$$E_a = E_0 \cos\left(\frac{\pi x}{a}\right)\hat{z} \tag{4.10}$$

$$\vec{E^i} = E_\theta\hat{\theta} + E_\phi\hat{\phi} \tag{4.11}$$

$$E_\theta = C\cos(\phi)\frac{\pi}{2}\frac{\sin(Z)}{Z}\frac{\cos(X)}{\left(\frac{\pi}{2}\right)^2 - (X)^2} \tag{4.12}$$

$$E_\phi = -C\cos(\theta)\sin(\phi)\frac{\pi}{2}\frac{\sin(Z)}{Z}\frac{\cos(X)}{\left(\frac{\pi}{2}\right)^2 - (X)^2} \tag{4.13}$$

where :

$$
\begin{aligned}
C &= jkabE_0 \frac{e^{jkr_i}}{2\pi r_i} \\
X &= k\frac{a}{2}\sin\theta\sin\phi \\
Z &= k\frac{a}{2}\sin\theta\cos\phi
\end{aligned}
\tag{4.14}
$$

k being the wavenumber and r_i, θ and ϕ the coordinates of the observation point in the spherical system centred on the aperture (Fig.(4.3)).

4.5. Oblique incidence: the electric field

The $\vec{E^i}$ radiated by the source antenna in far field conditions is orthogonal to the propagation vector $\vec{r_i}$. The preliminary considerations presented in the section (4.3) allow to represent whatever $\vec{E^i}$ in *TE* and *TM* components.

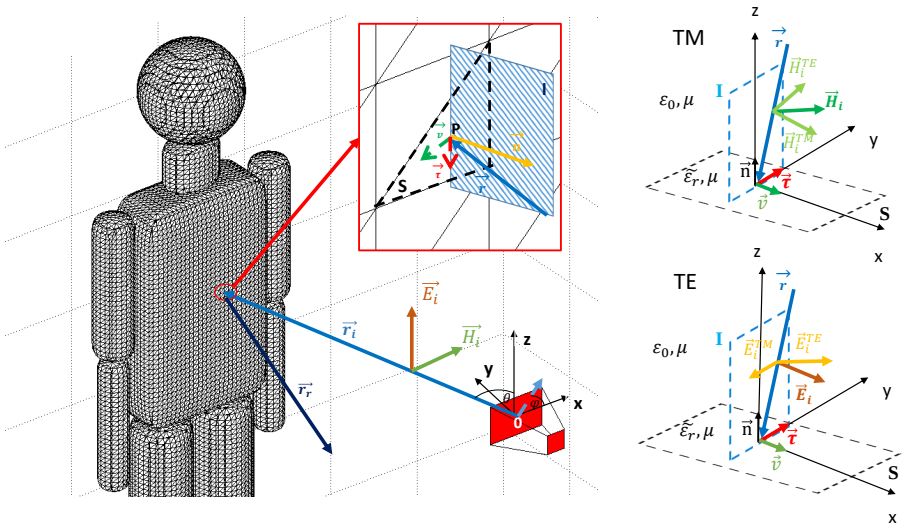

Figure 4.5.: Body scattering

The *TE* component is the field component perpendicular to the incidence plane (Fig.(4.5))

$$
\vec{E}_\perp = \vec{E}^{TE} = \left(\vec{E}\cdot\hat{v}_\perp\right) \tag{4.15}
$$

It follows that the TM field component in the incidence plane is

$$\vec{E}_{\parallel} = \vec{E}^{TM} = \vec{E}^{i} - \vec{E}^{TE} \tag{4.16}$$

The field radiated by the aperture impinges on the surface S from the incident direction $\hat{r_i}$ and it is partially reflected in the direction $\hat{r_r}$, as a shown in Fig. (Fig.(4.5)). The reflected field is calculated considering the oblique incidence of a plane wave on an interface between two dielectric media [69]. In detail, TE and TM are reflected by the surface S with two different reflection coefficients, ρ^{TE} and ρ^{TM}. Assuming the surface of the medium characterized by a relative permittivity ϵ_r and conductivity σ, the expressions of the reflection coefficients are:

$$\cos\theta_i = -\hat{n}\cdot\hat{r} \tag{4.17}$$

$$\rho^{TE} = \frac{\cos\theta_i - \sqrt{\left(\epsilon_r - \frac{j\sigma}{\omega\epsilon_0}\right) - 1 + \cos^2\theta_i}}{\cos\theta_i + \sqrt{\left(\epsilon_r - \frac{j\sigma}{\omega\epsilon_0}\right) - 1 + \cos^2\theta_i}} \tag{4.18}$$

$$\rho^{TM} = \frac{\sqrt{\left(\epsilon_r - \frac{j\sigma}{\omega\epsilon_0}\right) - 1 + \cos^2\theta_i} - \left(\epsilon_r - \frac{j\sigma}{\omega\epsilon_0}\right)\cos\theta_i}{\sqrt{\left(\epsilon_r - \frac{j\sigma}{\omega\epsilon_0}\right) - 1 + \cos^2\theta_i} + \left(\epsilon_r - \frac{j\sigma}{\omega\epsilon_0}\right)\cos\theta_i} \tag{4.19}$$

θ_i being the incidence angle. The total electric field tangential to the surface S and due to the TE components is given by the contribution of the incident and reflected waves, so combining eq.(4.15) and eq.(4.18), its expression is:

$$\vec{E}^{TE}_{tan} = \left(1+\rho^{TE}\right)E^{TE}_{x}\hat{x} + \left(1+\rho^{TE}\right)E^{TE}_{y}\hat{y} + \left(1+\rho^{TE}\right)E^{TE}_{z}\hat{z} \tag{4.20}$$

The $\vec{E}^{TM}$ field is not tangential to the surface S, so the component of the incident field tangential to the surface from (4.9) and (4.16) is calculated

$$\vec{E}^{TM}_{\tau} = \left(\vec{E}^{TM}\cdot\hat{\tau}\right)\hat{\tau} \tag{4.21}$$

Using (4.19), the total electric field tangential to the surface and due to the TM component is given by the contribution of the incident and reflected waves

$$\vec{E}^{TM}_{tan} = \left(1+\rho^{TM}\right)E^{TM}_{\tau_x}\hat{x} + \left(1+\rho^{TM}\right)E^{TM}_{\tau_y} + \left(1+\rho^{TM}\right)E^{TM}_{\tau_z} \tag{4.22}$$

It follows that the electric field tangential to the surface S is the superposition

of the TE (4.20) and TM (4.22) components

$$\vec{E}_{tan}^{TOT} = \vec{E}_{tan}^{TE} + \vec{E}_{tan}^{TM} \tag{4.23}$$

4.6. Oblique incidence: the magnetic field

The magnetic incident field from the knowledge of the incident electric field $\vec{E}$ is calculated as

$$\vec{H}^i = \frac{\hat{r} \wedge \vec{E}}{\eta} = H_\theta \hat{\theta} + H_\phi \hat{\phi} \tag{4.24}$$

being η the free space wave impedance. The TM component is the magnetic component perpendicular to the incidence plane and tangent to the surface S

$$\vec{H}^{TM} = \left(\vec{H} \cdot \hat{v}_\perp\right) \hat{v}_\perp \tag{4.25}$$

The TE magnetic component in the incidence plane is

$$\vec{H}^{TE} = \vec{H}^i - \vec{H}^{TM} \tag{4.26}$$

The total magnetic field on the surface S and due to the TM component is given by the contribution of the incident and reflected waves, so combining eq.(4.25) and eq.(4.18)

$$\vec{H}_{tan}^{TM} = \left(1 - \rho^{TM}\right) H_x^{TM} \hat{x} + \left(1 - \rho^{TM}\right) H_y^{TM} \hat{y} + \left(1 - \rho^{TM}\right) H_z^{TM} \hat{z} \tag{4.27}$$

The $\vec{H}^{TE}$ is not tangential to the surface S, so at first it is necessary to compute the component of the incident field tangential to the surface by a scalar multiplying eq.(4.9) and eq.(4.26)

$$\vec{H}_\tau^{TE} = \left(\vec{H}^{TE} \cdot \hat{\tau}\right) \hat{\tau} \tag{4.28}$$

Using (4.19), the total electric field tangential to the surface and due to the TE component is given by the contribution of the incident and reflected waves

$$\vec{H}_{tan}^{TE} = \left(1 - \rho^{TE}\right) H_{\tau_x}^{TE} \hat{x} + \left(1 - \rho^{TE}\right) H_{\tau_y}^{TE} + \left(1 - \rho^{TE}\right) H_{\tau_z}^{TE} \tag{4.29}$$

This means that the magnetic field tangential to the surface S is the superposition of the TE (4.29) and TM (4.27) components

$$\vec{H}_{tan}^{TOT} = \vec{H}_{tan}^{TE} + \vec{H}_{tan}^{TM} \tag{4.30}$$

4.7. Radiation of the equivalent currents

The knowledge of the electric (4.23) and magnetic (4.30) fields tangential to the surface S allows to apply the equivalence theorem [70] to determine the equivalent electric **J** and magnetic **M** surface current densities flowing on the surface

$$\vec{J} = \hat{n} \wedge \vec{H}_{tan}^{TOT} \tag{4.31}$$

$$\vec{M} = \vec{E}_{tan}^{TOT} \wedge \hat{n} \tag{4.32}$$

The surface S is replaced by an equivalent Huygens' source in free space whose dimensions are small enough to consider the currents uniform throughout. This allows to calculate the scattered field as the field radiated by the equivalent currents $\vec{J}$ and $\vec{M}$. It follows that, defining the electric $\vec{A}$ and magnetic $\vec{F}$ vector potential

$$\vec{A} = \frac{\mu}{4\pi} \vec{J} \frac{e^{-j\beta R}}{R} S \tag{4.33}$$

$$\vec{F} = \frac{\epsilon}{4\pi} \vec{M} \frac{e^{-j\beta R}}{R} S \tag{4.34}$$

$$R = \sqrt{(x - x_p)^2 + (y - y_p)^2 + (z - z_p)^2} \tag{4.35}$$

At the observation point x,y,z, the electric field $\vec{E}^r$ radiated by the currents is

$$\vec{E}^r = \frac{\nabla \nabla \cdot \vec{A}}{j\omega\epsilon\mu} - j\omega\vec{A} - \frac{1}{\epsilon} \nabla \wedge \vec{F} \tag{4.36}$$

The sum of the fields radiated by the all subareas n represents the total field scattered by the body.

$$\vec{E}_{TOT}^r = \sum_{n=1}^{N} \vec{E}_n^r \tag{4.37}$$

4.8. Field received by the antenna of the observed target

The EM analytical model proposed was thought to define the parameters (*i.e.* operating frequencies or bandwidth of the antenna, distance, type of movements and others) at the design stage of systems, addressed for the remote monitoring of physiological and physical activities of people in domestic environments. In the previous works [25, 26, 71, 72], it was observed that the electric field scattered by the monitored subject gives a phase and magnitude variation of the total reflection coefficient S_{11} at the antenna input port. In practical situations this scattering parameter is easy to measure, so the theoretical model was developed in order to characterize the S_{11} term. The knowledge of the S_{11} allows to retrieve useful informations relative the vital signs and the physical activities of the observed human subject. Accordingly, it was calculated the total field scattered by the body (eq. (4.36) and eq.(4.37)) retrieved by the antenna in order to reproduce the real scenario. The knowledge of the signal received by the antenna makes it possible to evaluate the S_{11} scattering parameters [73]:

$$S_{11} = \frac{E^{r_z}_{TOT}}{E_0} \sqrt{\frac{\lambda^2 G}{4\pi a_1 b_1}} \tag{4.38}$$

where $E^{r_z}_{TOT}$ is the dominant z-component of the total received field (4.37), E_0 is the emitted electric field which is calculated with the knowledge of the radiated power [74]

$$P_{rad} = \frac{|E_0|^2 a_1 b_1}{240\pi} \tag{4.39}$$

and a_1, b_1 and G are the width, the height and the gain respectively of the antenna. It is evident from the eq. (4.38) that the features of the antenna allow the proper evaluation of the scattering parameter S_{11}. To this purpose the following section is dedicated to define the characteristics of the antenna, used in the laboratory tests, which are presented and discussed in the chapters (5) and (6).

4.9. Antenna

The antenna used in the laboratory tests is a Flann Standard Gain Horns (4.6), Model 16240, which works in the frequency range 8.20 - 12.40GHz. The specific dimensions are listed in the table (4.2).

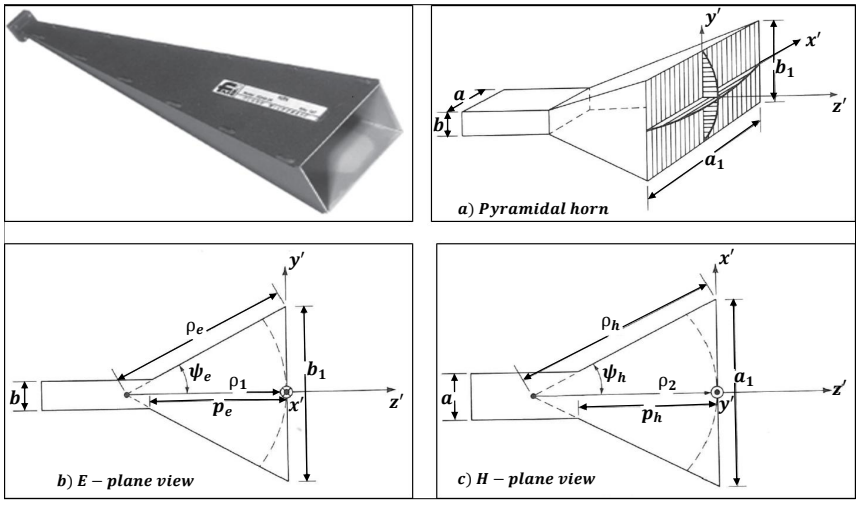

Figure 4.6.: Pyramidal horn antenna

Table 4.2.: Pyramidal horn antenna's dimensions

E-plane view		*H-plane view*	
p_e	23.08cm	p_h	23.08cm
ρ_e	26.78cm	ρ_h	29.08cm
b	1.02cm	a	2.29cm
b_1	7.9cm	a_1	10.9cm
ψ_e	8.48°	ψ_h	10.53°

Referring to the eq.(4.38), it seems clear that the gain G represents a paramount feature for the evaluation of the scattering parameters S_{11}.
The maximum gain is related to the directivity by [68]:

$$G_{MAX} = e_{cd} D_{MAX} \tag{4.40}$$

where e_{cd} is the antenna radiation efficiency. Since the antenna is stated to be

lossless, then the radiation efficiency

$$e_{cd} = 1 \tag{4.41}$$

As a consequence, the maximum gain corresponds to the antenna's directivity. The directivity of the pyramidal horn was computed using the following procedure [75].

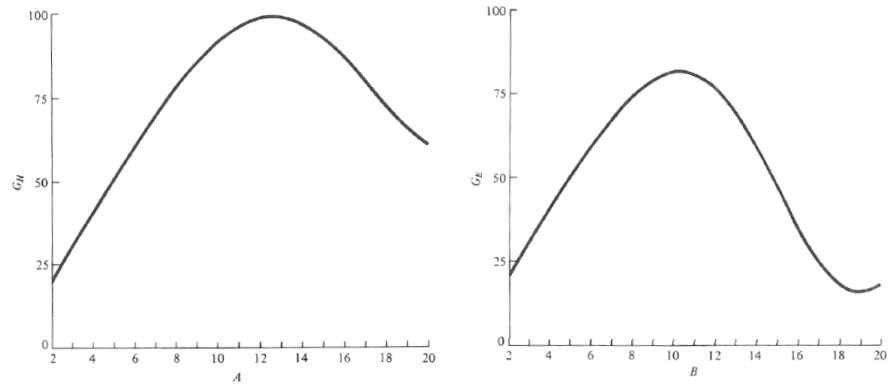

Figure 4.7.: G_E and G_H as a function of A and B respectively (SOURCE: Adopted from data by E. H. Braun, "*Some Data for the Design of Electromagnetic Horns*", *IRE Trans. Propagat.*, Vol. AP-4, No. 1 January 1956, IEEE)

It was calculated

$$A = \frac{a_1}{\lambda}\sqrt{\frac{50}{\frac{\rho_h}{\lambda}}} \tag{4.42}$$

$$B = \frac{b_1}{\lambda}\sqrt{\frac{50}{\frac{\rho_e}{\lambda}}} \tag{4.43}$$

Using A (4.42) and B (4.43), G_H and G_E were obtained respectively from the graphs showed in the Fig.(4.7)[1]. The directivity was finally calculated as

$$D = \frac{G_E G_H}{\frac{32}{\pi}\sqrt{\frac{50}{\frac{\rho_e}{\lambda}}}\sqrt{\frac{50}{\frac{\rho_h}{\lambda}}}} \tag{4.44}$$

[1]SOURCE: Pictures taken from C. A. Balanis, "*Antenna Theory: analysis and design*", *John Wiley & Sons*, 1997

In the following table (4.3), the values of the directivity are reported.

Table 4.3.: Pyramidal horn antenna's directivity

f (GHz)	A	B	G_E	G_H	D_p	$D_p(dB)$
8	7.38	5.57	70	56	52.28	17.58
10	8.25	6.23	78	63	89.75	19.53
12	9.04	6.83	80	67	117.45	20.70

The resulting gain for a lossless pyramidal horn antenna is shown in Fig. (4.8)

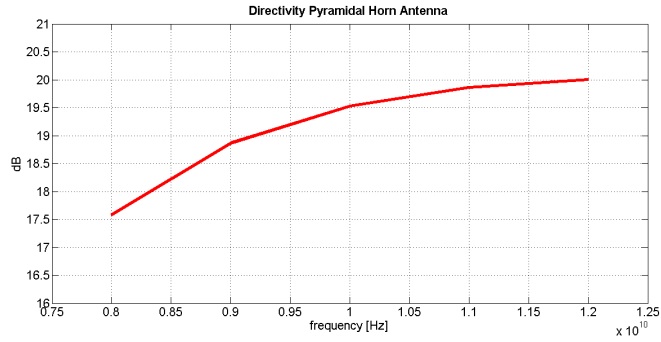

Figure 4.8.: Gain at *X-band* (8.2-12.4GHz) for a lossless pyramidal horn antenna

Chapter 5.

Static Target Analysis

In this chapter several tests have been performed to evaluate the accuracy and feasibility of the EM model and explained in the previous chapter (4), will be presented. In detail, measurements and simulations with the EM model (whose code was implemented in MATLAB [60]) were performed and compared for the following significant situations: 1) metallic sphere, 2) lossless homogeneous objects (sphere and cylinder), and 3) dielectric complex structures (mannequin and real target).

5.1. Evaluation of the RCS PEC Sphere: comparison with theoretical values

Radar cross section (RCS) is the measure of the power backscattered by a target to the source or in a given direction, normalised with respect to the power density of the incident field. Hence, it can be considered as an estimation of the radar efficiency, based on an energy measure of the echoes backscattered from a target toward the receiver. Formally, RCS is defined as [76]

$$\sigma = \lim_{R \to \infty} 4\pi R^2 \frac{\left|\vec{E}^r\right|^2}{\left|\vec{E}^i\right|^2} \tag{5.1}$$

where:

- σ is the radar cross section of the target (m^2);
- $\vec{E}^r$ is the reflected electric field (V/m) with the same polarisation of the receiving antenna;
- $\vec{E}^i$ represents the incident electric field (V/m);

- R is distance between the target and radar.

The purpose of the normalisation is to remove the effect of the range, making the cross section (*effective area*) independent from the distance between scattering object and radar (R) [76]. The efficiency depends on frequency, target configuration (*shape, size, material composition*) and other factors that vary widely between different types of target. Therefore with the aim to compare dissimilar objects, it is usual to express their efficiency in terms of the RCS of a perfectly conducting sphere (5.1) which returns the same power to the same receiver in the same conditions [77].

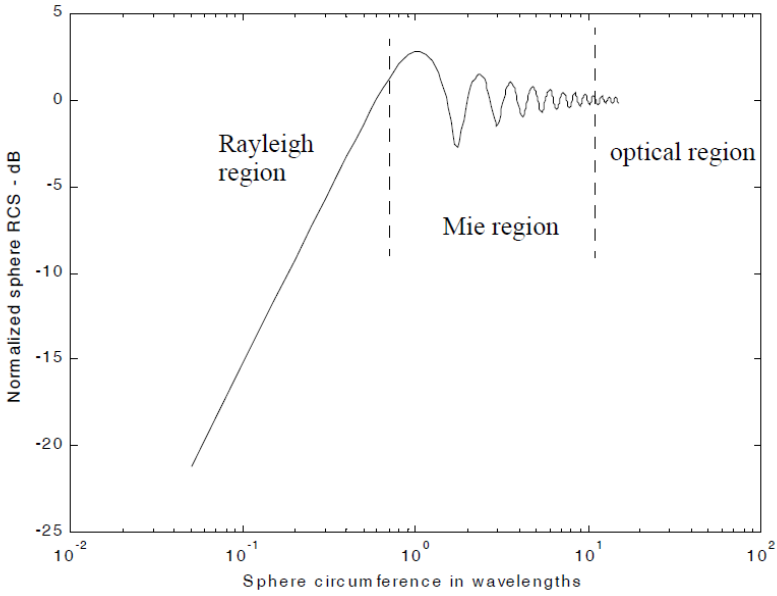

Figure 5.1.: Radar Cross-Section Diagram in semi-log scale of a metallic sphere (SOURCE: Adopted from data by B. R. Mahafza, "Radar systems analysis and design using MATLAB," *CRC press*, 2002.)

In the Fig. (5.1) the normalised backscattered RCS for a perfectly conducting sphere is represented as a function of its circumference in wavelength units ($ka = 2\pi a/\lambda$). Three regions are identified:

- **Rayleigh Region:** the sphere is small in relation with the wavelength ($2\pi a/\lambda << 1$), its RCS is proportional to fourth power of the frequency and is determined more by the volume of the scatterer than by its shape [78]

$$\sigma \simeq [\pi \mathrm{a}^2][7.11(\mathrm{ka})^4]$$

- **Mie (resonance) region:** the radar wavelength is comparable to the object's dimension ($2\pi a/\lambda \approx 1$) and RCS fluctuates due to the interference between the specular and creeping-wave contributions [79];

- **Optical Region:** The wavelength is small compared to target's dimension and RCS of a Sphere is independent of frequency ($2\pi a/\lambda > 1$). In this case the geometric optics approximation

$$\sigma = \pi^2 a;$$

is usually an adequate representation of the magnitude of the RCS.

Therefore, the first test was the evaluation of the RCS of a perfectly conducting sphere, replacing in the eq. (5.1) the incident electric field $\vec{E}^i$ and that backscattered by the sphere $\vec{E}^{r_z}_{TOT}$, calculated respectively by (4.10) and (4.37). The presented EM model reproduced a sphere of a radius 12cm, placed in far field distance of 20m away from the antenna, and the analysis of the RCS σ was performed in the frequency range 250MHz-16GHz. The results are reported in Fig. (5.2)

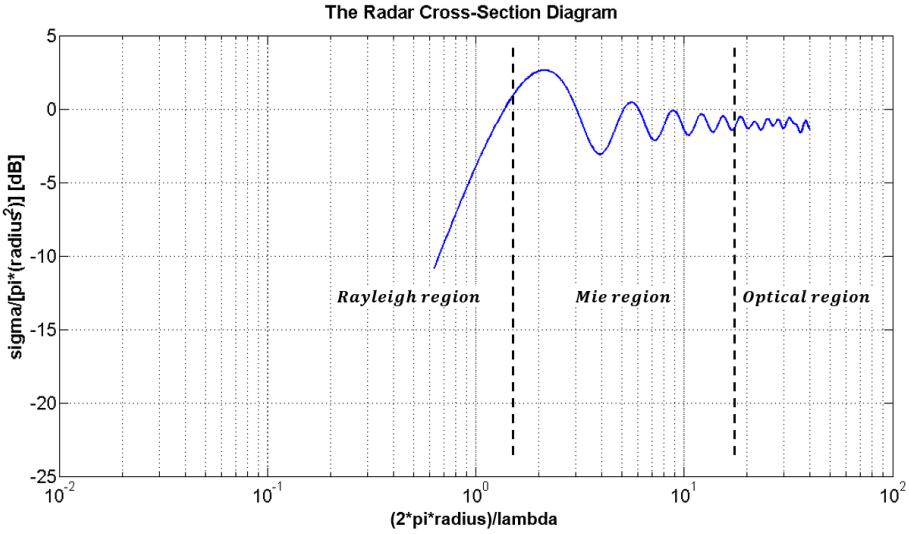

Figure 5.2.: Normalised RCS for a perfectly conducting sphere using semi-log scale, evaluated with the proposed model

The results demonstrate how the EM model based on PO approach is able to estimate with accuracy of 1-2dB the electric field impinging on the sphere and diffracted by itself, necessary for the evaluation of the relative RCS. In the Fig. (5.2) the three regions mentioned above are well outlined with good agreement with the peak values observed in the Fig. (5.1).

5.2. Evaluation of the scattering parameter due to a PEC sphere: comparison with measurements

A further test was carried out to validate experimentally the EM model, evaluating the scattering parameter S_{11} relative to a metallic sphere. Measurements were performed in an anechoic chamber at *École CentraleSupélec*, with the collaboration of *SONDRA* research group, during a internship abroad of the author.

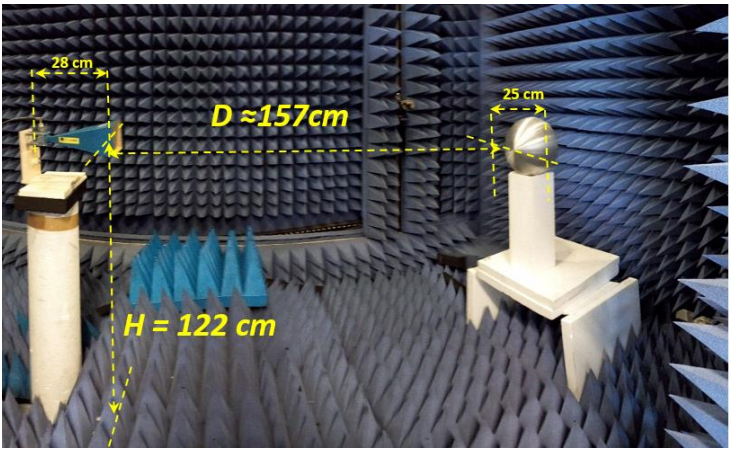

Figure 5.3.: S_{11} measurement set-up used for the characterisation of a PEC sphere placed at 157cm away from the horn antenna

Fig. (5.3) shows the measurement system composed by:

- PEC sphere (*radius 25cm*) placed at distance D ≈ 157cm away from the antenna;

- Horn pyramidal antenna (8.2–12.4GHz frequency range) whose features are explained in detail in the section (4.9);

- Pyramidal microwave absorbers;

- Vector Network Analysser (*VNA*) for the generation of the signal, with frequency centre f_c 10.3GHz and bandwidth 500MHz, in the frequency range 10.05-10.550GHz.

The same setup was implemented in the model, generating the sphere of radius 25cm through the eq. (4.1) and setting its properties $\epsilon_r = 1$ and $\sigma = 10^7 S/m$ in order to emulate the behaviour of a metallic surface. The reflection coefficient S_{11} was calculated from the eq. (4.38), taking in account the features of the horn antenna in the work frequencies chosen (4.9). The comparison between the measured and simulated S_{11} is presented in Fig. (5.4).

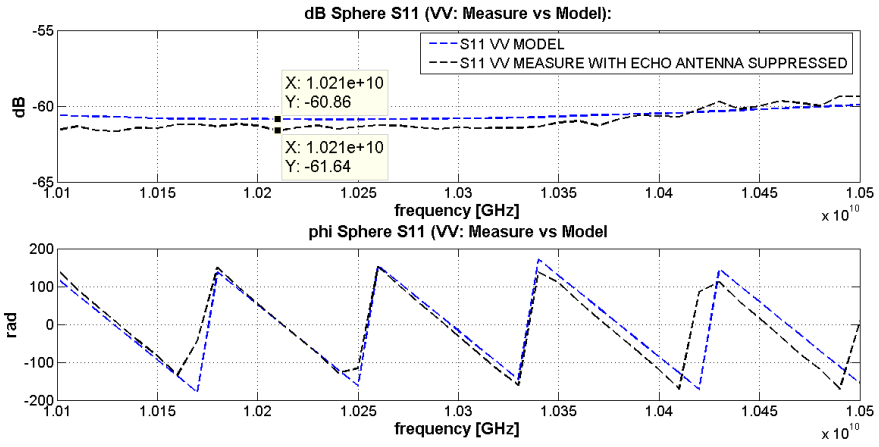

Figure 5.4.: Comparison between the measured and simulated S_{11} of a PEC sphere distant 157cm away from the antenna: modulus (top), phase (bottom)

The Figure (5.4) shows a good agreement between the simulated S_{11} (blue dashed line) and measured S_{11} (black dashed line); these values were obtained subtracting the contribution of the antenna to S_{11}, and therefore they represent the contribution of the sphere only. The EM model is able to provide a S_{11} value equal to what expected and observed in the measurement, and a difference smaller than 1dB, as far as the amplitudes profile is concerned, can be ascribed to measurement uncertainty. A good correspondence is well highlighted also in time domain, applying the inverse Fourier transform to the simulated and measured signal, as shown in Fig. (5.5)

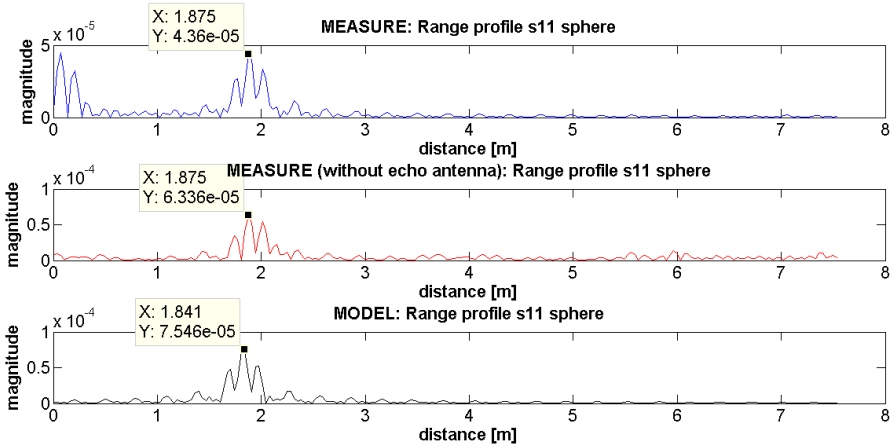

Figure 5.5.: Time domain: comparison between the measured and simulated S_{11} of a PEC sphere distant 157cm away from the antenna

The EM model is able to provide a time domain response whose waveform and peak values are in good agreement with experimental data.
The same agreement between the measured and simulated results was observed changing the position of the sphere (distance D $\approx$ 250cm away from the antenna), as displayed in Fig. (5.6):

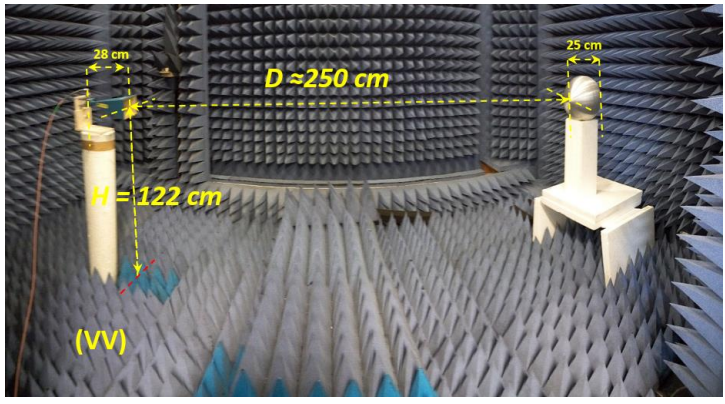

Figure 5.6.: S_{11} measure of a PEC sphere placed at 250cm away from the horn antenna

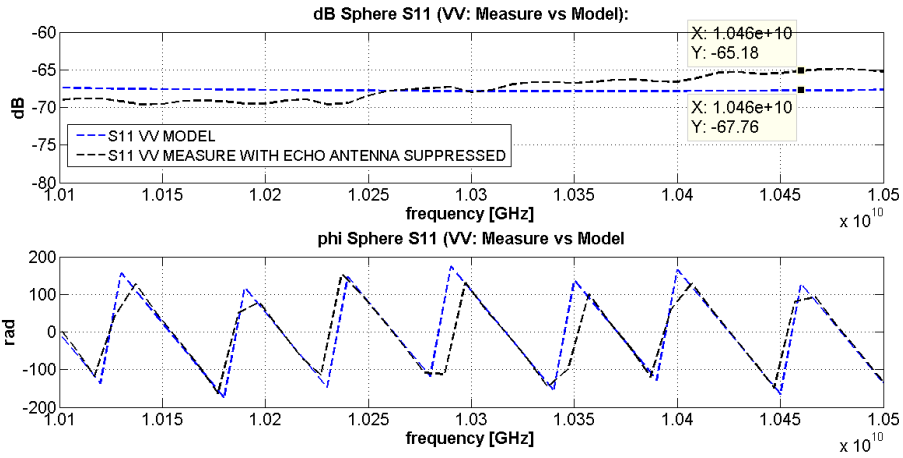

Figure 5.7.: Comparison between the measured and simulated S_{11} of a PEC sphere distant 250cm away from the antenna

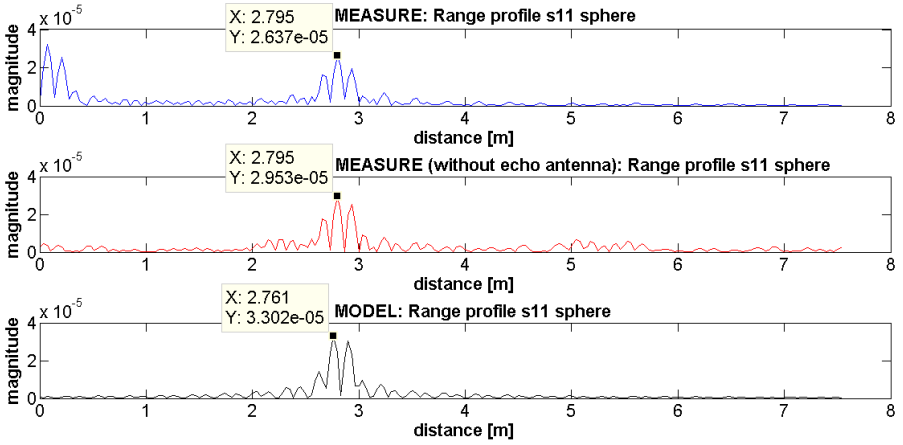

Figure 5.8.: Time domain: comparison between the measured and simulated S_{11} of a PEC sphere distant 250cm away from the antenna

5.3. Evaluation of the scattering parameter due to a PEC cylinder: comparison with measurements

In the *Antenna laboratory* of the *Department of Information Engineering* at UNIVPM a measure of the scattering parameter S_{11} was performed, relative to a metallic cylinder, in the frequency range 8.5-11.5GHz. The goal was to observe the accuracy of the EM model to evaluate the S_{11} in the total work frequencies of the adopted antenna for a different kind of geometry respect to the sphere.

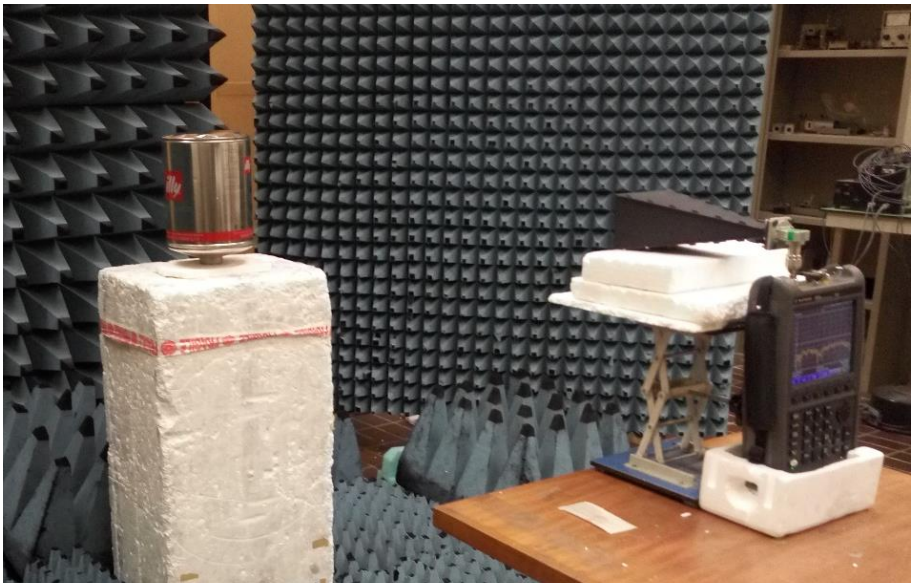

Figure 5.9.: S_{11} measurement set-up of a PEC cylinder

Figure (5.9) shows the system composed by:

- PEC cylinder (radius 11cm, height 26cm) placed at distance D $\approx$ 200cm away from the antenna;
- Horn pyramidal antenna (8.2–12.4GHz frequency range);
- Pyramidal microwave absorbers;

- Vector Network Analysser (*VNA*) for the generation of the signal, with frequency centre f_c 10.5GHz and bandwidth 3GHz, in the frequency range 8.5-11.5GHz.

The same setup was implemented in the model, following the same procedure executed for the calculation of the S_{11} of the sphere. The comparison between the measured and simulated results is shown in Fig. (5.10):

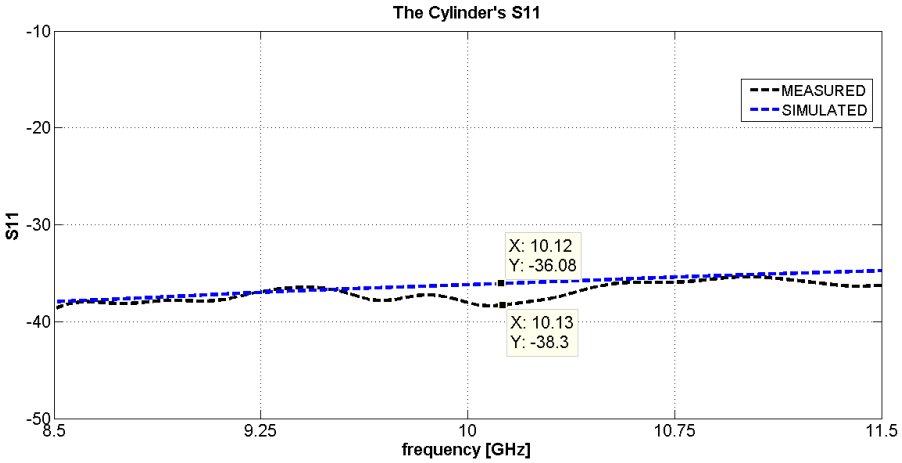

Figure 5.10.: Comparison between the measured and simulated S_{11} of a PEC cylinder distant 200cm away from the antenna

The Fig. (5.10) shows a good agreement between the simulated S_{11} and the measured result, observing at most a difference of 2dB in correspondence of the centre frequency. This can be associated to the fact that the measure was not carried out in a fully anechoic environment, thus it is affected by the environment reflections that corrupt the quality of the result.

5.4. Evaluation of the scattering parameter due to a phantom: comparison with measurements

The EM model was stressed with a further test, evaluating the S_{11} of a mannequin which presents a more complex structure than that of the sphere or of the cylinder mentioned above. The mannequin is usually used in dosimetry applications and is characterise by a lossy dielectric material.

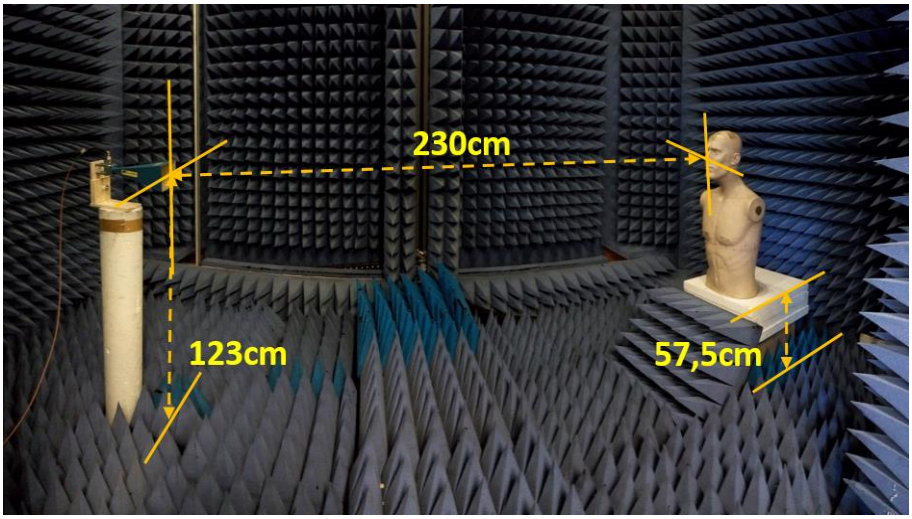

Figure 5.11.: S_{11} measurement set-up of a mannequin filled by a lossy dielectric material

Fig. (5.11) shows the system composed by:

- Mannequin filled with water, placed at distance D $\approx$ 230cm away from the antenna;
- Horn pyramidal antenna (8.2–12.4GHz frequency range);
- Pyramidal microwave absorbers;
- Vector Network Analysser (*VNA*) for the generation of the signal, with frequency centre f_c 10.3GHz and bandwidth 500MHz, in the frequency range 10.05-10.550GHz.

In the EM model the mannequin was designed with an equivalent phantom where head, neck and torso are rappresented by sphere, cylinder and parallelepiped as shown in the Fig. (5.12)

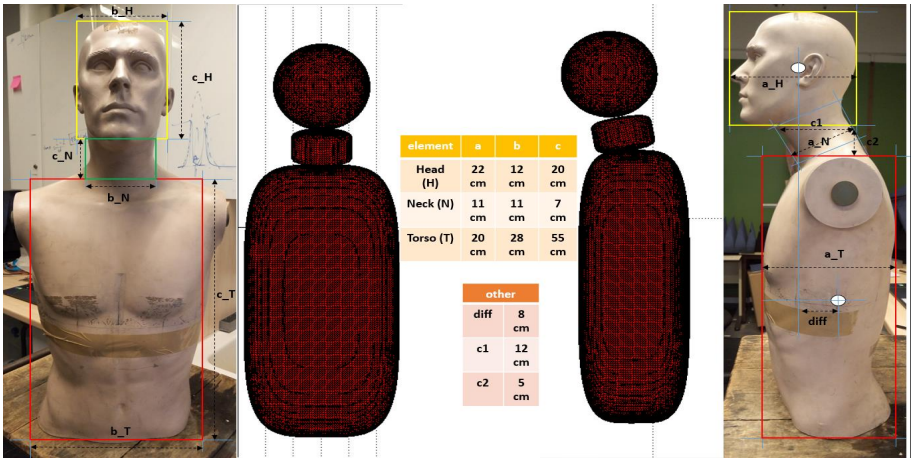

Figure 5.12.: Mannequin reproduced by sphere, cylinder and parallelepiped, implemented in MATLAB

As regards the dielectric properties, taking in account the frequency/temperature-dependent behaviour of the complex relative permittivity of the water [80] (Fig. (5.13))

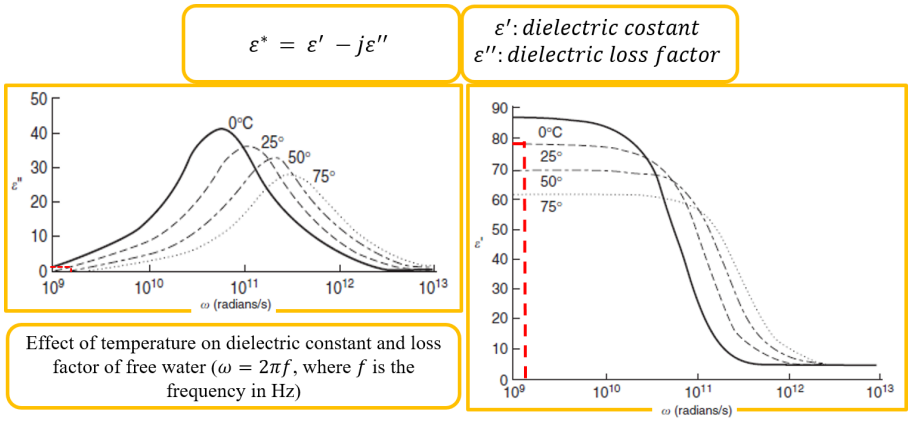

Figure 5.13.: Frequency-temperature dependence of the complex relative permittivity

A dielectric constant $\epsilon^{'} = 76$ and a dielectric loss factor $\epsilon^{''} = 2.76$ were chosen, for the centre frequency 10.3GHz, assuming a work temperature of

25°. The comparison between the measured and simulated result is depicted in Fig. (5.14):

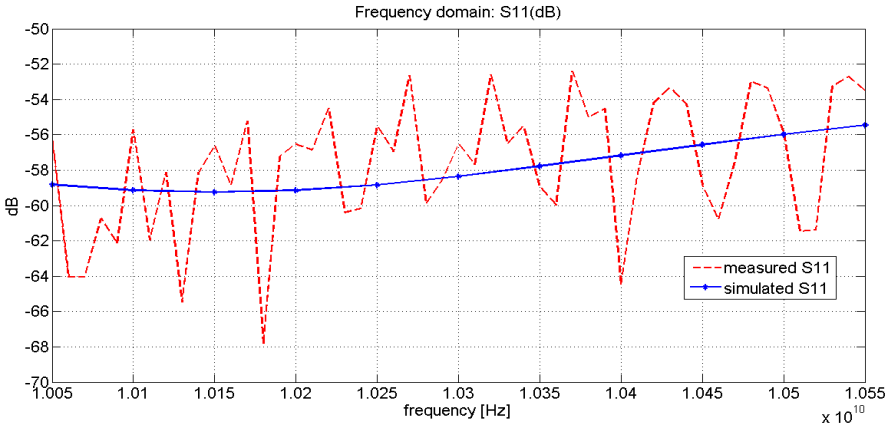

Figure 5.14.: Comparison between the measured and simulated S_{11} of a mannequin distant 230cm away from the antenna

In the Fig. (5.14), the dashed red line represents the measured S_{11} which is characterise by an evolution strongly oscillatory respect to the monotonic increasing of the simulated S_{11}, continuous blue line. Nevertheless, the response predicted by the model can be considered in qualitatively good agreement with the measure, being close between the maximum and minimum peak value of the measured S_{11} for all the frequency range analysed.

5.5. Evaluation of the scattering parameter due to a real target: comparison with measurements

In the last test a real target was considered to compare the scattering parameter achieved through a measure and the corresponding simulation with the proposed EM model.

Figure 5.15.: S_{11} measurement set-up of a real target

As depicted in Fig. (5.15), the system is composed by:

- Volunteer at distance D $\approx$ 200cm away from the antenna;
- Horn pyramidal antenna (8.2–12.4GHz frequency range);
- Pyramidal microwave absorbers;
- Vector Network Analysser (VNA) for the generation of the signal, with frequency centre f_c 10GHz and bandwidth 4GHz, in the frequency range 8-12GHz.

In the numerical model, the body parts were modeled by sphere, cylinders and parallelepiped (Fig. (4.1)), whose dimensions are reported in the Table (4.1).

Refering to section (3.1), the dielectric properties of the skin were chosen ($\epsilon_r = 33.5$ and $\sigma = 8.9 S/m$ [57], relative to the selected frequency regims), assuming that only the external layer is interested by the fields. The comparison between measured and simulated result is presented in Fig. (5.16)

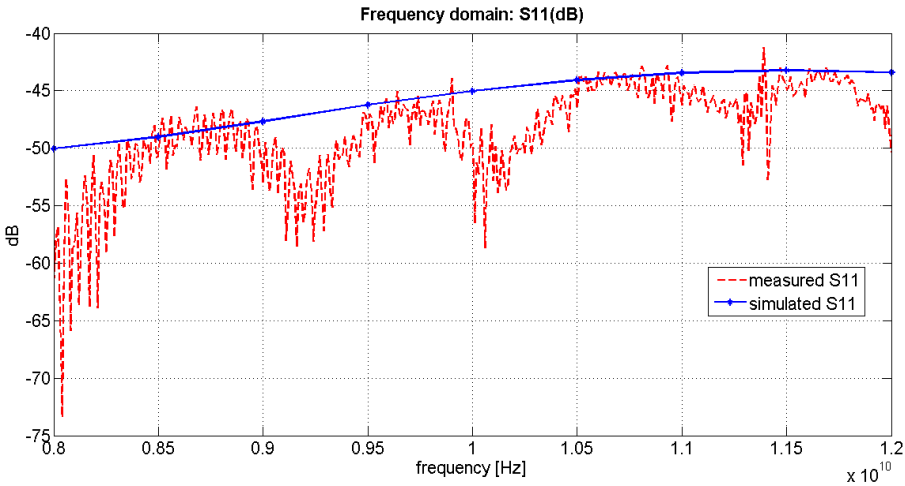

Figure 5.16.: Comparison between measured and simulated S_{11} measure of a real target

It can observe an oscillatory increasing behaviour of the measured result (dashed red line), respect the regular trend (dashed blue line) of the phantom data, simulated with the model, quite similar to the results observed in the analysis of the mannequin. This may be associated to the multiple reflections in a not perfect anechoic environment and the error about the value of the dielectric properties of the body. Nevertheless the response of the model well follows the increasing evolution of the measured result, with an agreement within 1-2dBs about the peak value observed in the red line. Moreover, it is important highlight that the purpose of the EM model proposed is to analyse qualitatively and quantitatively the general physical activity of a monitored subject. In this kind of studies, that will be discuss in the following chapter (6), the contributions of the static objects and static part of the human body are subtracted, in order to highlight the harmonic content of the corresponding moving parts, and consequently some critical aspects take a lesser importance.

The performances of the EM model proved to be extremely satisfying in terms of computational burden and calculation time. All scenarios reproduced in Matlab required approximately 2s for each analysed frequency with a total

simulation time of few minutes for each test. In conclusion, all performed tests show that the model is a reliable and accurate tool to simulate the field scattered by a human body close to an antenna.

Chapter 6.

Moving Target Analysis

The EM model was developed to support the proper design of contact-less sensors, addressed to the remote monitoring of the physiological and physical activities of a patient. The acquisition in real time of both information allows a well-timed assessment of the health state of the monitored subject in indoor environment. The human body activities can be classified by using *micro-Doppler* radar systems, that are able to detect small variations in the carrier frequency caused by non-rigid-body motions [81, 82]. Several studies were carried out for identification and classification of different human activities [56, 83–85], where the micro-Doppler features were extracted through several time-frequency analyses such as *Short-Time Fourier Transform (STFT)* [86, 87]. Usually, full wave numerical methods (*Method of Moments (MoM)* enhanced with *Fast Multipole Method (FMM)*) were used to analyse the micro-Doppler signature of a moving target [81]. The aim of this research was to perform Doppler analysis of a human moving subject, starting by the frequency signature achieved by the analytical EM model proposed in this thesis. The study and the implementation of the Doppler techniques were conducted in *SONDRA (Supelec Onera NUS DSO Research Alliance)* at CentraleSupélec, with the supervision of *ONERA*, during the study period of the author.

In detail in this chapter, the oscillation of a pendulum in front of the antenna and the movement forward and backward of one arm of a real target were analysed and discussed, preceded by the description of the synthetic array data processing, implemented in the model to retrieve the relative Doppler information.

6.1. Radar signature analysis

In order to analyse qualitatively and quantitatively the physical activities of a subject, as well as to discriminate the individual contributions of the moving body parts, Fast Fourier Transform (FFT) and Short-Time Fourier Transform (STFT) were used to observe the relative Doppler information. The procedure implemented in the model is shown in Fig. (6.1), following similar criteria described by V. Chen in [86]. Defined an observation time, for each time interval Δt, a frequency sweep was performed, with M frequencies equidistant of Δf (Fig. (6.1)-*a)*). The total bandwidth B determines the radar range resolution ($\Delta R = \frac{c}{2B}$, c being the speed of light); the total N performed frequency sweeps, in the total observation time, determine the Doppler or the cross-range resolution. The signal reflected by the moving target is shifted in frequency by an amount proportional to the velocity of the object (Fig. (6.1)-*b)*). The frequency shift f_D, called *Doppler frequency* and the speed of relative motion are related through the following formula:

$$f_D = \frac{-2v\cos\theta}{\lambda} \tag{6.1}$$

where θ is the angle between the main axis of the radar and the direction of the target's movement, v is the speed of the target and λ is the wavelength of the transmitted electromagnetic signal.
The total returned signal is demodulated at baseband and the resulting $M \times N$ complex data (Fig.(6.1)-*c)*), is organised into a two-dimensional array, which represents the unprocessed spatial frequency signature of the target $S(f_{m,n})$ (m = 0,1,...,M-1, n = 0,1,...,N-1). Then, M-point Inverse Fourier Transform (IFT) was performed for each N received frequency signatures, obtaining N range profiles, each containing M range cells. This operation allows to observe the target's reflectivities in range (Fig. (6.1)-*d)*). In order to retrieve the Doppler information of a moving target, an FFT for each M range cell was executed, generating a M-by-N image which depicts the target's reflectivities, mapped into the range-Doppler plane (Fig. (6.1)-*e)*). Usually, the received signal relative to a complex or irregular motion is a wide spectrum of frequencies which are time-varying. This kind of data does not lend itself well to Fourier analysis, which can cause a large amount of smearing in the frequency domain. The fast Fourier transform indicates which frequency components are contained in the signal but not how the frequencies change with time. For this reason it was implemented the STFT, which proves to be an efficient way to resolve the image blurring problem due to the time-varying Doppler's behaviour.

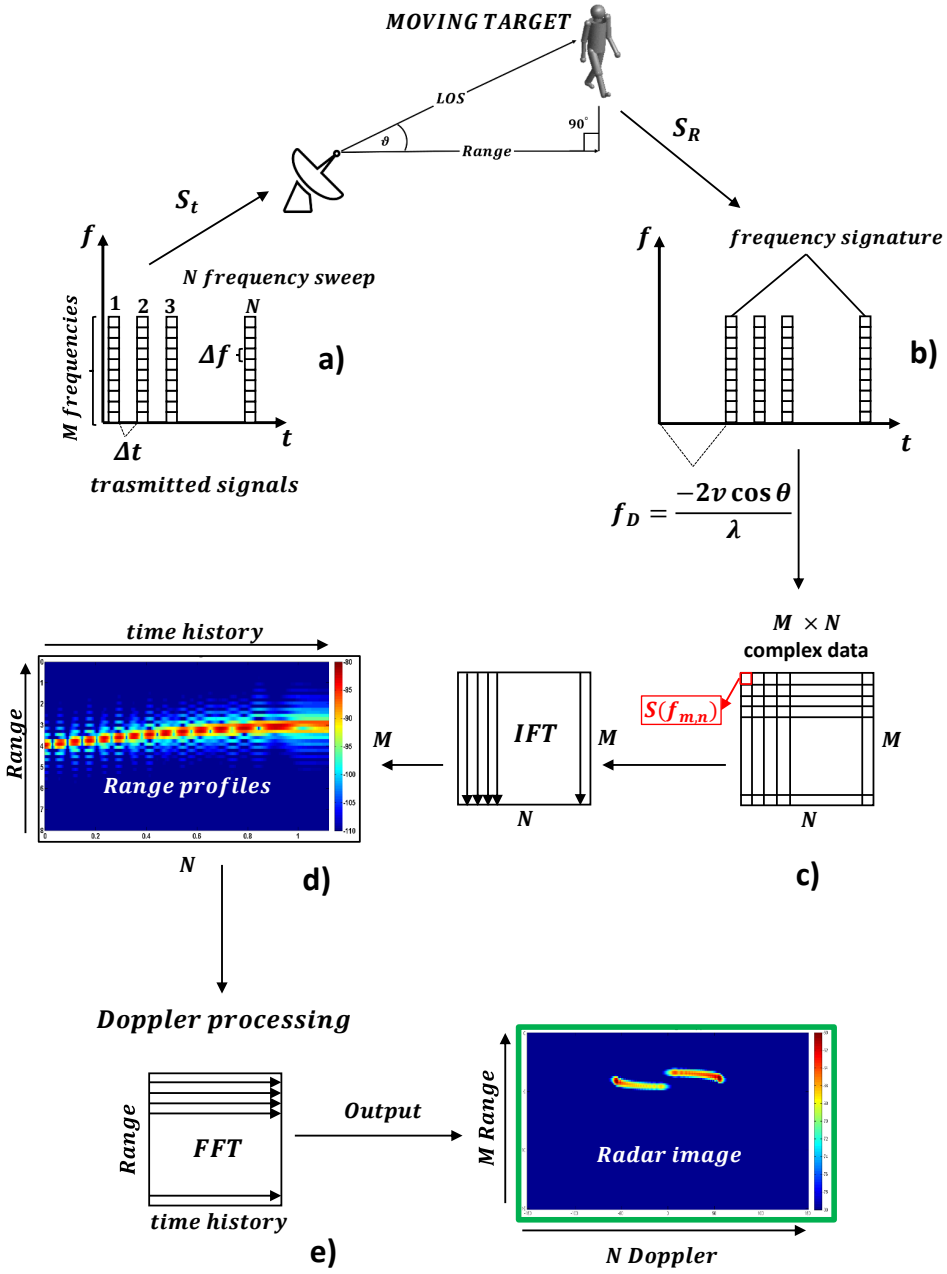

Figure 6.1.: Radar imaging of a moving target using FFT

The STFT is a time-frequency transform defined as:

$$STFT(t,\omega) = \int_{\infty}^{\infty} s(\tau)w(\tau - t)e^{-j\omega\tau}d\tau \tag{6.2}$$

where *s(t)* is the signal, *w(t)* is a short-time window function which limits the resolution of the STFT. Indeed there is a trade-off between the time resolution and the frequency resolution. A larger window has higher frequency resolution but lower time resolution. Therefore, starting from the range profiles (Fig. (6.2)) a STFT was performed for each time history series, generating a $N \times N$ time-Doppler distribution. By combining the M time-Doppler distributions at M cells, the $N \times M \times N$ time-range-Doppler cube was formed. Consequently, there are N image frames and every one represents a full range-Doppler image in a particular time instant.

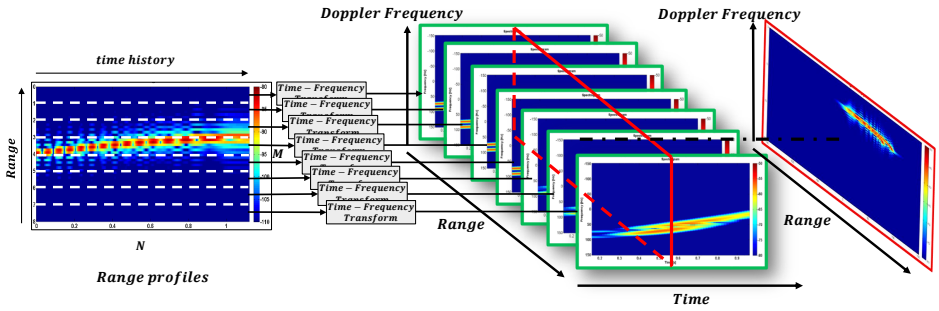

Figure 6.2.: Radar imaging of a moving target using STFT

6.2. Doppler signature of a pendulum made up of two spheres

In order to verify the accuracy of the procedure explained in the previous section, a pendulum made up of two spheres was reproduced by the analytical EM model and Doppler informations relative to its oscillation were analysed. In detail, two spheres (*blu* and *red*) of radius 24cm were reproduced, placed at distance of 4m and 5m respectively from the rotation point A, and separated by a distance of 1m, as shown in Fig. (6.3)

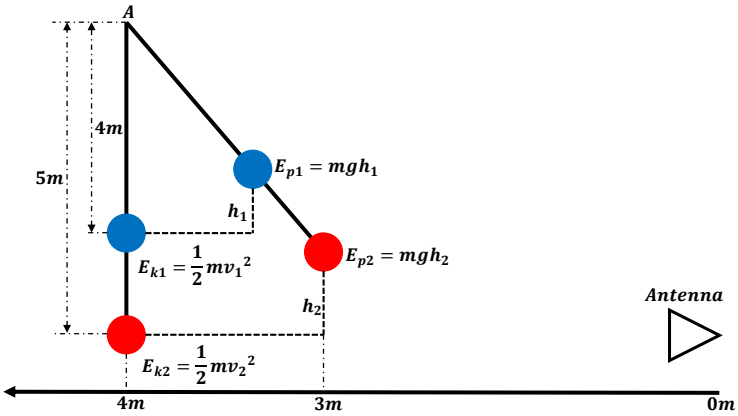

Figure 6.3.: Oscillation of pendulum made up of two sphere

Only one half swing forward was analysed in an observation time of 1,12s, corresponding to a translation of 1m, starting at a distance of 4m from the antenna. 16 frequencies, from 10.225GHz to 10.375GHz, were transmitted with an integration time Δt of 0.003s. The bandwidth of the resulting transmitted signal is equal to 150MHz which allows to achieve 1m of range resolution. The aim was to test the reliability of the EM model to reproduce the distribution in range of the reflected signals of the two spheres and their Doppler frequencies mapped into range-Doppler and time-Doppler plane. To this purpose, it was calculated every Δt the S_{11} of the total system by the eq. (4.38), for each transmitted frequency. Following the procedure explained in the previous section (Fig. (6.1)-*c*), the range profile of the returned signal was obtained as shown in Fig. (6.4)

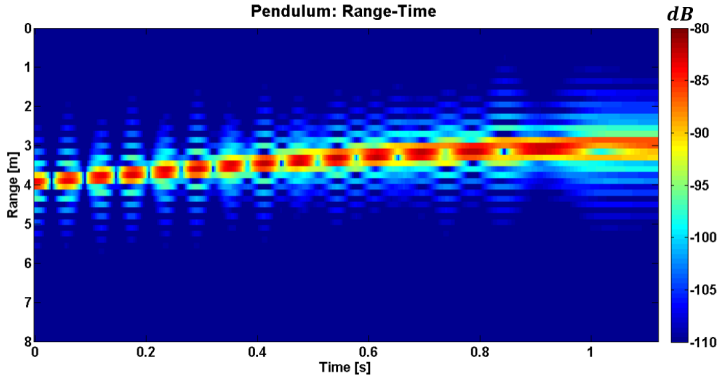

Figure 6.4.: Range profile of the signal reflected by the pendulum

The total displacement of the pendulum is well outlined, from the starting position of 4m to the final position of 3m respect the antenna. Whereas, the individual positions of the two spheres are not well detected due to the adopted range resolution, comparable with the distance between them.
Referring to the system shown in the Fig. (6.3), the maximum expected Doppler frequencies are 76Hz and 95.5Hz, respectively for the blue and red sphere, calculated following the eq. (6.1).

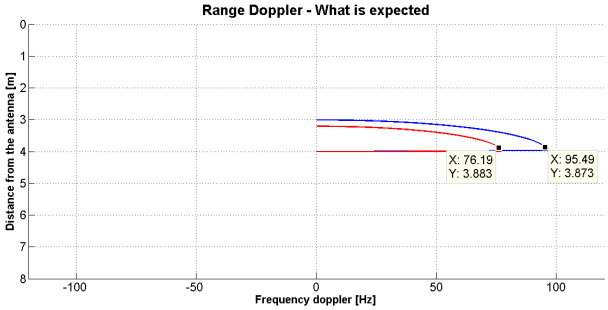

Figure 6.5.: Doppler frequencies theoretically calculated

The Fig. (6.5) depicts all the expected frequencies shift of the reflected signal, due to the swing forward of the two spheres in the chosen observation time. The distributions of the Doppler frequencies in range was calculated through the analytical model, performing the FFT as explained in the section (6.1) and shown in Fig. (6.1)-*d*).

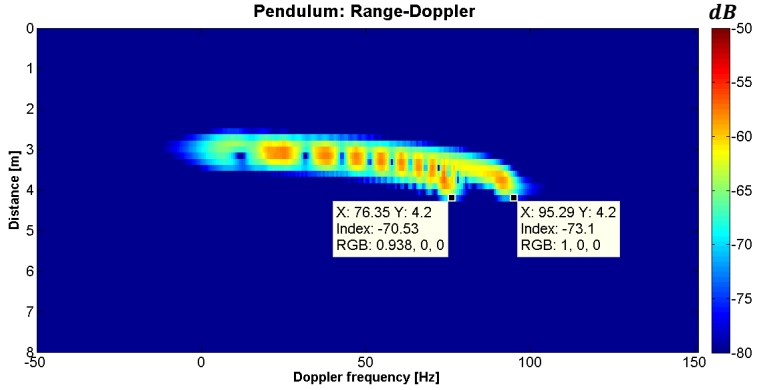

Figure 6.6.: Range-Doppler distribution of the signal reflected by the pendulum

The Fig. (6.6), represents the range-Doppler image relative to the swing of the pendulum. The maximum Doppler frequencies of 76Hz and 95.5Hz are well detected, showing an excellent agreement between simulated results and the values theoretically calculated. Nevertheless the range-Doppler plane appears blurred in the frequency range 0-50Hz, due to the range resolution. This doesn't allow to discriminate the individual Doppler profiles in range, when the swinging spheres decrease their velocity.
The reflectivities of the swinging pendulum were also observed in time, performing a STFT, following the procedure explained in section (6.1) and shown in Fig. (6.2)). To this purpose, a sampling rate of 300Hz, a sliding window of 100 points, an overlap of 9/10, and a Hamming window were used.

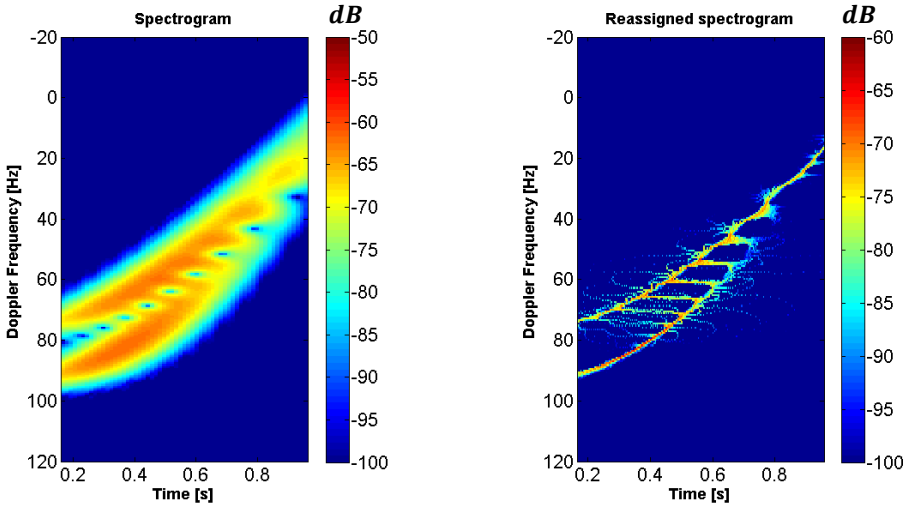

Figure 6.7.: Time-Doppler distribution of the signal reflected by the pendulum for the range 3-4m

Fig. (6.7) shows the spectrogram relative to the range 3-4m where the Doppler profiles of the two spheres are well highlighted for the total observation time. The adopted range resolution allowed to border the Doppler effect at a range where the total displacement is expected. In the time-Doppler image the two spheres are well detected and discriminated by their own Doppler frequencies whose values are perfectly in agreement with the values theoretically calculated and shown in Fig. (6.5). The time-frequency representation is limited by the tradeoff between the resolution in time and frequency, dependently by the chosen size of the moving window. In order to avoid this issue, a *Time-frequency reassignment* was used. Whereas the STFT represents the energy in a partic-

ular windowed signal, as a set of point estimates on the time-frequency lattice (with parameters determined by the block length and overlap), time-frequency reassignment shifts these coefficients away from the lattice to the centre of gravity of the windowed energy [88]. The readability of the resulting spectrogram proves to be improved and the Doppler frequencies are detected accurately, as shown in Fig. (6.7).

Further test was carried out considering a different scenario. The range-Doppler and time-Doppler analysis were performed by the EM model, relative to two swinging spheres which move one forward (*red sphere*) and the other backward (*blue sphere*) the antenna, as shown in Fig. (6.8)

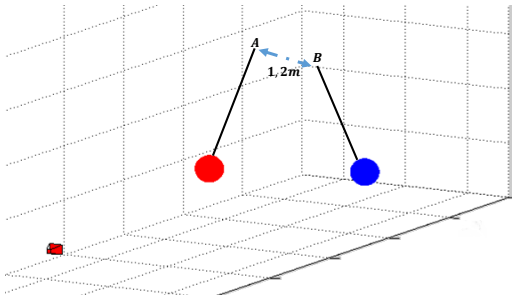

Figure 6.8.: Swinging spheres forward and backward respect the antenna's direction

In detail, two spheres (blu and red) of radius 24cm were reproduced by the model, placed at distance of 5m from the rotation points A and B, and separated from each other by a distance of 1,2m. It was analysed only one half swing forward of the red sphere, and one half swing backward of the blue sphere, observing for each a total translation of 0.6m, starting from a distance of 4m from the antenna. An observation time of 1,12s was chosen and 51 frequencies, from 10.05GHz to 10.55GHz, were transmitted with an integration time Δt of 0.003s. The bandwidth of the resulting transmitted signal is equal to 500MHz which allows to achieve 0.3m of range resolution. Referring to the system shown in the Fig. (6.8), the maximum estimated frequencies Doppler are $\pm 56.5 Hz$, whose sign depends on the target's direction movement (positive if the target is moving away the radar, negative in opposite case).

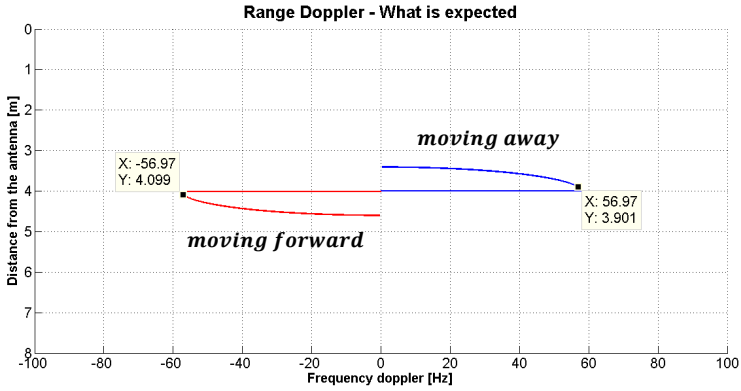

Figure 6.9.: Doppler frequencies theoretically calculated of two swinging spheres

The Doppler frequencies of the swinging spheres were calculated using the analytical model, performing the FFT for each row of the received complex data (Fig. (6.1)-d)). The result is shown in Fig. (6.10).

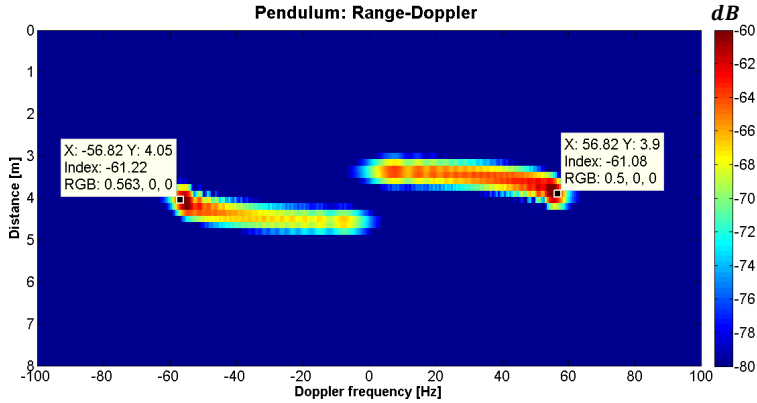

Figure 6.10.: Range-Doppler distribution of the signal reflected by the two swinging spheres

The shifted frequencies due to the different swings of the spheres are well highlighted and the image shows an excellent agreement with the Doppler profiles theoretically calculated and depicted in the Fig. (6.9). Moreover the EM model proves to be accurate for the calculation of the scattered fields intensities, in fact the signals reflected by the red sphere is stronger than that reflected by the blue sphere, coherently with what expected.

In the end, the time-Doppler analysis was performed, applying a STFT, with a sampling rate of 300Hz, a sliding window of 100 points, an overlap of 9/10, and a Hamming window. Due to the adopted range resolution it was need to retrieve several time-Doppler images to observe the total displacement of the two sphere, being not the relative Doppler effect confined in a single range cell, as shown in the following Fig. (rif fig)

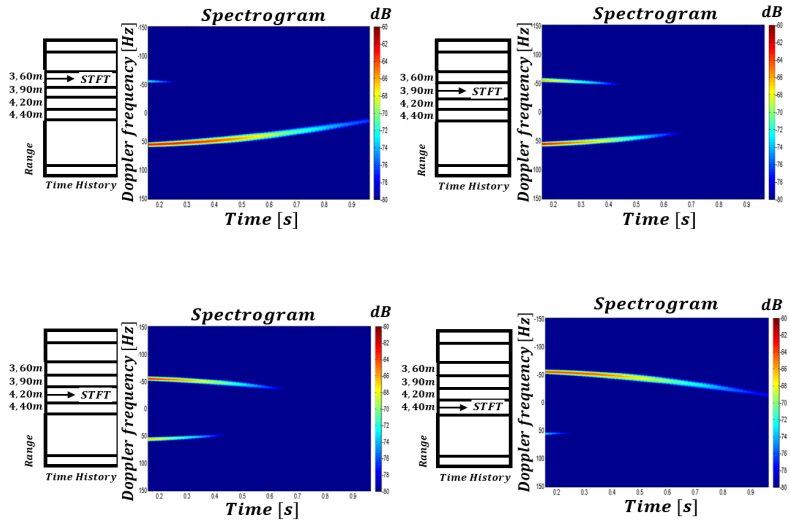

Figure 6.11.: Time-Doppler distribution of the signal reflected by the two swinging spheres

The Fig. (6.11) shows a final result in total agreement with what shown in the Fig. (6.9). The Doppler frequencies are were outlined and detected in greater detail through the Time-frequency reassignment.

6.3. Evaluation of the Doppler signature of a moving real target: comparison with measurement

Once demonstrated in section (6.2) the accuracy and the reliability of the EM model to perform Doppler analysis, in this section will be presented an experimental validation of the analytical model, that was carried out considering a moving human target. In particular, the Doppler informations relative to the swings of a human's arm were extracted, performing join time-frequency analysis on measured and simulated data.

The laboratory set up consisted of a portable Vectorial Network Analyser (VNA) and a horn pyramidal antenna which operated in CW. This choice was due to the limitations of the available instruments that didn't allow to acquire data adopting a frequency sweep with a proper sampling frequency. The antenna radiated a signal at frequency of 10GHz with a power level of 0dBm. The subject was located at a distance of 2m in front of the antenna, which was placed 1.30 m above the ground. The backscattered field was acquired in real time by the VNA at the sampling frequency of 150Hz. The volunteer was asked to continuously move his right arm forward and backward respect the antenna direction, during a time interval of 10s. The STFT was then applied to the measured data, to generate the corresponding spectrogram shown in Fig. (6.12)

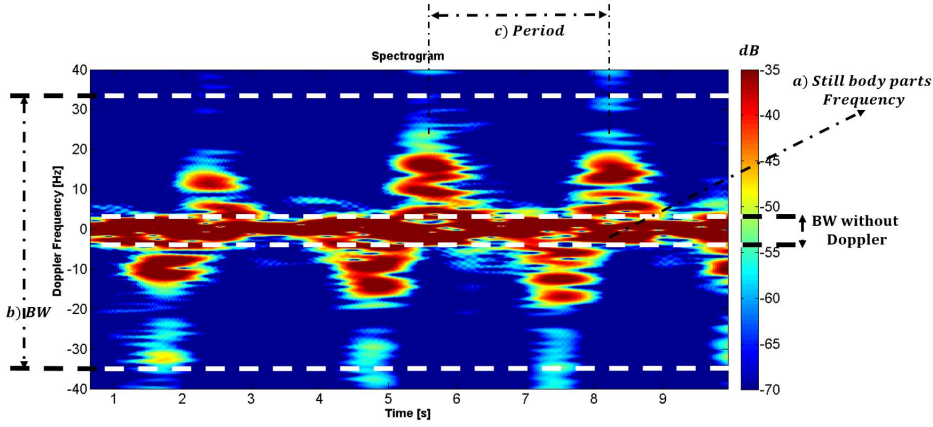

Figure 6.12.: Measured spectrogram relative to the swings of a human's arm

The measured signal is the combined reflection from all the body components that induce a wide spectrum of frequencies, strongly time-varying. The resulting spectrogram, depicted in Fig. (6.12), shows distinct signatures depending on the activity. The strongest return comes from the torso and the still human body parts (Fig. (6.12) - *a)*), while the arm swings introduces a Doppler shift determining the total bandwidth BW of the Doppler signal (Fig. (6.12) - *b)*). In the figure, 3 complete arm swings are well highlighted, during the total observation time of 10s, with a cadence time of about 2.7s (Fig. (6.12) - *c)*).
The experimental test was simulated using the model, and the human body model proposed in the section (5.5). Obviously, despite the real human movement is continuous, it was necessarily simulated as a sequence of frameworks corresponding to different arm positions $(0°, 0° + \Delta\theta, ..., 90°;)$. Pictures of the

experiment were used to synchronise the virtual movements of the arm with the measurement scenario. STFT and Time-frequency reassignment were then applied to generate the corresponding spectrograms, presented in the follow Fig. (6.13)

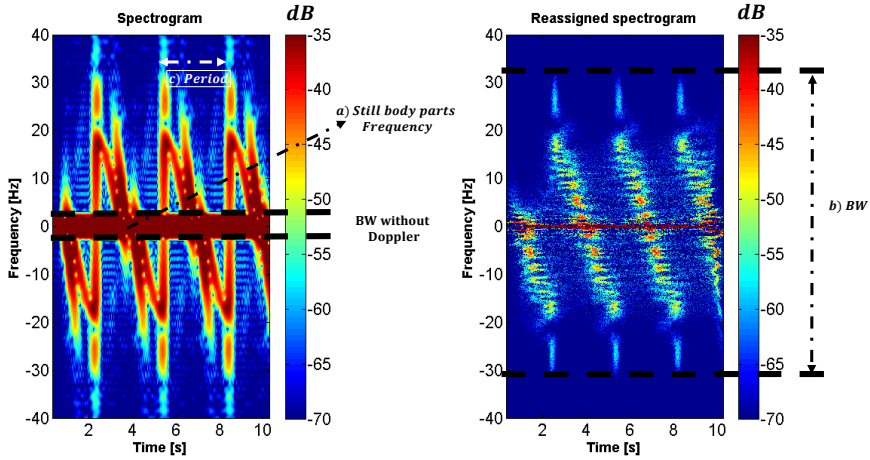

Figure 6.13.: Simulated spectrogram relative to the swings of a human's arm

The Time-frequency reassignment was performed to eliminate the artefacts due to the construction of the arm's movement in the model, and to discriminate accurately the Doppler frequencies of the moving body parts.
Accordingly to measured results, in the Fig. (6.13) two distinct signatures are observed: the strongest return of the still body parts (Fig. (6.13) - a)) and the sawtooth modulation introduced by the movements of the arm (Fig. (6.13) - b)). The tree complete swings are well detected with a cadence time of 2.7s as observed in the experimental result (Fig. (6.13) - c)). The simulated spectrogram shows constant ascendant and descendent arms movements which are not observed in the measured spectrogram due to the involuntary movements of the volunteer. Moreover it is possible to observe a good agreement between the measured and simulated result as regard the total bandwidth of the Doppler signal, and the maximum Doppler frequency detected, approximately equal to 31Hz.
Therefore, the experimental investigation shows the accuracy of the code and confirms the actual possibility of using the proposed analytical model to acquire useful information about the general activity of a target, performing Doppler analysis.

Chapter 7.

Conclusions and Suggestions for Future Development

The analytical EM model described in this thesis was developed and implemented in MATLAB, in order to characterise the fields diffracted by a human body. The model allows to investigate, by means of PO approach, the interactions between the EM waves and the body, and to analyse how some parameters such as the work frequencies, the distances, or the movements of a target, affect the fields scattered by a monitored subject. These features are useful for the proper design of the EM sensors addressed to the remote monitoring in AAL applications.

First of all, it was demonstrated that, from an EM point of view in the few range of GHz, the mutual coupling among the body parts and the anatomical details can be neglected. Consequently, the 3D human model was developed replacing the human body parts with elementary shapes, with a good resolution and without any significant distortion of the backscattered waveform. This approach makes the EM model light from the computational burden a point of view, and more efficient than the widely used numerical tools, which usually face the complexity and massive memory involved in the detailed modelling of the human body.

Several tests were carried out to validate the analytical model, proposing different scenarios. The comparison between experimental and numerical data proves that the EM model can accurately evaluate the scattering parameter S_{11}, analysing both lossless homogeneous objects that dielectric complex structures.

Doppler techniques were studied, analysed and implemented in the proposed model in order to detect general activities of a human subject. To this purpose, an experimental test on a moving target was carried out and simulated by the EM model, to validate the accuracy of the implemented code. The comparison showed the ability of the analytical model to faithfully reproduce the real scenario and to distinguish the different body parts of the moving subject by their Doppler frequencies.

The use of the proposed EM model allows to optimise the design of unobtrusive sensor (setting dimensions, range frequency and positioning in indoor environments), for remote monitoring of physiological an physical activity of elderly people. This future generation of contact-less devices paves the way for increasing patients' well being and personal independence. To this purpose, further investigations will concern the characterisation and estimation of several postures and the instantaneous velocity of the moving subject for the fall detection. Falls are a major public health concern and main causes of accidental death in the senior population. Timely and accurate detection permits immediate assistance after a fall and, thereby, reduces complications of fall risk. Moreover, it may be interesting to classify different physical activities of a subject, analysing the relative Doppler frequencies, in order to detect the involved energy expenditure.
AAL is not the only research field where the proposed model can be applied. For example, in recent years in military context, there was a increasing need to locate and monitor individuals in a forest which represents an important component for border security. Consequently many researches are focused on measuring and classifying human micro-Doppler features in forested environments. In this context the EM model seems to be suitable to investigate and reproduce human motions in a FoPen (Foliage Penetration) configuration.
A further research field is represented by the GPR applications, e.g. the detection of buried subjects. In this context the model may be suitable for the good knowledge of the EM fields diffracted by people beneath rubble. These kinds of studies could provide an useful tool to detect the presence of breathing or heart activity of alive people trapped under earthquake rubble.

Appendix A.

Vector Transformations

In this appendix it is presented the vector trasformations from rectangular-to-spherical (and vice-versa). The coordinate system in shown in Fig. (A.1)

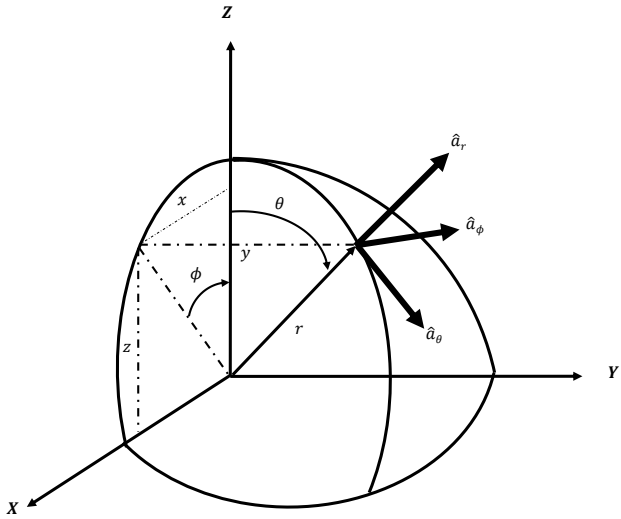

Figure A.1.: Spherical coordinate system

A.1. Rectangular-to-Spherical (and Vice-versa)

In the proposed analytical model it may be required that a transformation be performed directly from rectangular-to-spherical components.

In the rectangular coordinate system it expresses a vector $\mathbf{A}$ as

$$\mathbf{A} = \hat{a}_x A_x + \hat{a}_y A_y + \hat{a}_z A_z \tag{A.1}$$

where $\hat{a}_x$, $\hat{a}_y$ and $\hat{a}_z$ are the unit vectors and A_x, A_y and A_z are the component of the vector A in the rectangular coordinate system. By referring to Fig. (A.1) it can write that the rectangular and spherical coordinates are related by

$$\begin{aligned} x &= r\sin\theta\sin\phi \\ y &= r\cos\theta \\ z &= r\sin\theta\cos\phi \end{aligned} \tag{A.2}$$

and the rectangular and spherical components by

$$\begin{aligned} A_r &= A_x\sin\theta\sin\phi + A_y\cos\theta + A_z\sin\theta\cos\phi \\ A_\theta &= A_x\cos\theta\sin\phi - A_y\sin\theta + A_z\cos\theta\cos\phi \\ A_\rho &= A_x\cos\phi - A_z\sin\phi \end{aligned} \tag{A.3}$$

In matrix form, (A.3) can be written as

$$\begin{pmatrix} A_r \\ A_{theta} \\ A_\phi \end{pmatrix} = \begin{pmatrix} \sin\theta\sin\phi & \cos\theta & \sin\theta\cos\phi \\ \cos\theta\sin\phi & -\sin\theta & \cos\theta\cos\phi \\ \cos\phi & -\sin\phi & \end{pmatrix} \begin{pmatrix} A_x \\ A_y \\ A_z \end{pmatrix} \tag{A.4}$$

with the rectangular-to-spherical transformation matrix being

$$[A]_{rs} = \begin{pmatrix} \sin\theta\sin\phi & \cos\theta & \sin\theta\cos\phi \\ \cos\theta\sin\phi & -\sin\theta & \cos\theta\cos\phi \\ \cos\phi & -\sin\phi & \end{pmatrix} \tag{A.5}$$

The transformation matrix (A.5) is also orthonormal so that its inverse can be written as

$$[A]_{rs} = [A]_{rs}^{-1} = [A]_{rs}^{t} = \begin{pmatrix} \sin\theta\sin\phi & \cos\theta\sin\phi & \cos\phi \\ \cos\theta & -\sin\theta & -\sin\phi \\ \sin\theta\cos\phi & \cos\theta\cos\phi & 0 \end{pmatrix} \tag{A.6}$$

and the spherical-to-rectangular components related by

$$\begin{pmatrix} A_x \\ A_y \\ A_z \end{pmatrix} = \begin{pmatrix} \sin\theta\sin\phi & \cos\theta\sin\phi & \cos\phi \\ \cos\theta & -\sin\theta & -\sin\phi \\ \sin\theta\cos\phi & \cos\theta\cos\phi & 0 \end{pmatrix} \begin{pmatrix} A_r \\ A_\theta \\ A_\phi \end{pmatrix} \tag{A.7}$$

or

$$\begin{aligned} A_x &= A_r \sin\theta \sin\phi + A_\theta \cos\theta \sin\phi + A_\phi \cos\phi \\ A_y &= A_r \cos\theta - A_\theta \sin\theta \\ A_z &= A_r \sin\theta \cos\phi + A_\theta \cos\theta \cos\phi - A_\phi \sin\phi \end{aligned} \tag{A.8}$$

Appendix B.

Grid refinement study

The dimensions of the mesh has to be chosen such that the incident electric field $\vec{E}^i$ can be considered constant in the whole surface. In the GHz frequency region, the longitudinal direction of the discretising cell is electrically large structure in most case. Hence, several cells per wavelength λ are required to model the target and to decrease the numerical dispersion error. One significant issue in numerical computations is what level of grid resolution is appropriate. This is a function of type of analysis, geometry, and other variables. Ordinarily, it starts with a grid resolution and then conducts a series of grid refinements to assess the effect of grid resolution. This is known as a grid refinement study [89–91].
Accordingly, implementing the EM model in MATLAB (section (4)), a metal plate was reproduced, whose dimensions are $\lambda \times \lambda$, placed at 2m from the antenna, in order to define the proper dimension of the cell respect to λ.

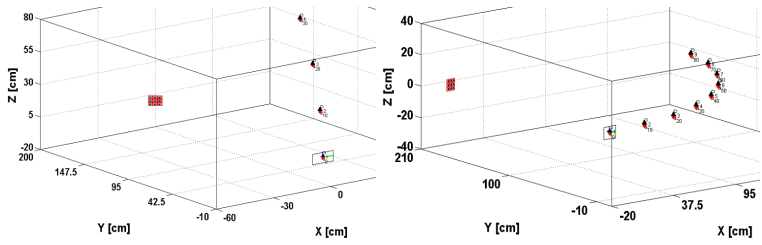

Figure B.1.: Discretised metal plate 2D

In correspondence of several observation points (Fig. (B.1)), the reflected field $\vec{E}^{r_z}_{TOT}$ (eq. (4.37)) was calculated, for a frequency $f = 4GHz$, refining each time the discretisation grid, until the computed solution is no longer changed and achieved an asymptotic value (Fig (B.2)).

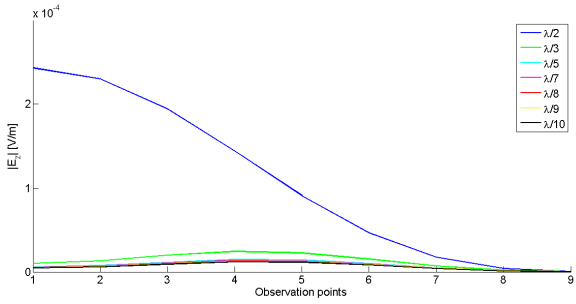

Figure B.2.: Reflected E field in different observation points

The same procedure was adopted for each rotation executed by the plate respect to the x, y and z axes whose results are listed in the table (B.1).

Table B.1.: Minimum requested dimensions cell

Rotation angle	*Horizontal plane view*			*Vertical plane view*		
	$x-axis$	$y-axis$	$z-axis$	$x-axis$	$y-axis$	$z-axis$
0°	$\lambda/4$	$\lambda/3$	$\lambda/4$	$\lambda/2$	$\lambda/2$	$\lambda/2$
10°	$\lambda/5$	$\lambda/3$	$\lambda/7$	$\lambda/3$	$\lambda/2$	$\lambda/3$
20°	$\lambda/6$	$\lambda/3$	$\lambda/8$	$\lambda/3$	$\lambda/2$	$\lambda/3$
30°	$\lambda/8$	$\lambda/3$	$\lambda/10$	$\lambda/4$	$\lambda/2$	$\lambda/5$
40°	$\lambda/9$	$\lambda/3$	$\lambda/10$	$\lambda/4$	$\lambda/2$	$\lambda/7$
50°	$\lambda/10$	$\lambda/3$	$\lambda/10$	$\lambda/6$	$\lambda/2$	$\lambda/8$
60°	$\lambda/10$	$\lambda/3$	$\lambda/10$	$\lambda/8$	$\lambda/2$	$\lambda/9$
70°	$\lambda/10$	$\lambda/3$	$\lambda/10$	$\lambda/8$	$\lambda/2$	$\lambda/10$
80°	$\lambda/10$	$\lambda/3$	$\lambda/10$	$\lambda/10$	$\lambda/2$	$\lambda/10$

It follows that, as not lie in the numerical dispersion problem and considering the several spatial orientations of the body respect to the antenna, the minimum value of each cell must to be at least equal to $\frac{\lambda}{10}$. This was the dimension used in the model presented in this Ph.D. thesis.

Bibliography

[1] "Global health and aging - national institute on aging," Available at: http://www.who.int/ageing/publications/global_health/en, Lastchecked February 2017.

[2] "Ageing -world health organization (who)," Available at: http://www.who.int/topics/ageing/en, Lastchecked February 2017.

[3] T. J. Hodgetts, "The identification of risk factors for cardiac arrest and formulation of activation criteria to alert a medical emergency team," *Resuscitation*, vol. 54, no. 2, pp. 125–131, 2002.

[4] M. Cretikos, *An evaluation of activation and implementation of the medical emergency team system.*, Ph.D. thesis, University of New South Wales, 2006.

[5] "National heart, lung and blood institute," Available at: http://www.nhlbi.nih.gov/health/health-topics/topics/sleepapnea, Lastchecked February 2017.

[6] R. Wolk, A. S. Gami, A. Garcia-Touchard, and V. K. Somers, "Sleep and cardiovascular disease," *Current problems in cardiology*, vol. 30, no. 12, pp. 625–662, 2005.

[7] R. S. Leung, M. E. Bowman, T. M. Diep, G. Lorenzi-Filho, J. S. Floras, and T. D. Bradley, "Influence of cheyne-stokes respiration on ventricular response to atrial fibrillation in heart failure," *Journal of Applied Physiology*, vol. 99, no. 5, pp. 1689–1696, 2005.

[8] T. L. Lee-Chiong Jr. and U. Magalang, "Monitoring respiration during sleep," *Respiratory care clinics of North America*, vol. 11, no. 4, pp. 663–678, 2005.

[9] "National confidential enquiry into patient outcome and death. An acute problem?," Available at: http://www.ncepod.org.uk/2005.htm, Lastchecked February 2017.

[10] K. Hillman, J. Chen, M. Cretikos, R. Bellomo, D. Brown, G. Doig, S. Finfer, and A. Flabouris, "Introduction of the medical emergency team (met)

system: a cluster-randomised controlled trial," *Lancet*, vol. 365, no. 9477, pp. 2091–2097, 2005.

[11] M. Cretikos, R. Bellomo, K. Hillman, J. Chen, S. Finfer, and A. Flabouris, "Respiratory rate: the neglected vital sign," *Medical Journal of Australia*, vol. 188, no. 11, pp. 657, 2008.

[12] M. R. Neuman, H. Watson, R. S. Mendenhall, J. T. Zoldak, J. M. Di Fiore, M. Peucker, T.M. Baird, D. H. Crowell, T. T. Hoppenbrouwers, D. Hufford, C. E. Hunt, M. J. Corwin, L. R. Tinsley, D. E. Weese-Mayer, and M. A. Sackner, "Cardiopulmonary monitoring at home: the chime monitor," *Physiological measurement*, vol. 21, no. 1, pp. 267, 2001.

[13] L. G. Lindberg, H. Ugnell, and P. A. Oberg, "Monitoring of respiratory and heart rates using a fibre-optic sensor," *Medical and Biological Engineering and Computing*, vol. 30, no. 5, pp. 533–537, 1992.

[14] K. Nakajima, T. Tamura, and H. Miike, "Monitoring of heart and respiratory rates by photoplethysmography using a digital filtering technique," *Medical engineering & physics*, vol. 18, no. 5, pp. 365–372, 1996.

[15] G. Matthews, B. Sudduth, and M. Burrow, "A non-contact vital signs monitor," *Critical Reviews in Biomedical Engineering*, vol. 28, no. 1 & 2, 2000.

[16] G. B. Moody, R. G. Mark, A. Zoccola, and S. Mantero, "Derivation of respiratory signals from multi-lead ecgs," *Computers in cardiology*, vol. 12, no. 1985, pp. 113–116, 1985.

[17] D. Dobrev and I. Daskalov, "Two-electrode telemetric instrument for infant heart rate and apnea monitoring," *Medical engineering & physics*, vol. 20, no. 10, pp. 729–734, 1999.

[18] X. Zhu, W. Chen, T. Nemoto, Y. Kanemitsu, K. Kitamura, K. Yamakoshi, and D. Wei, "Real-time monitoring of respiration rhythm and pulse rate during sleep," *IEEE transactions on biomedical engineering*, vol. 53, no. 12, pp. 2553–2563, 2006.

[19] S. Ansari, K. Ward, and K. Najarian, "Motion artifact suppression in impedance pneumography signal for portable monitoring of respiration: an adaptive approach," *IEEE Journal of Biomedical and Health Informatics*, 2016.

[20] D. Shao, Y. Yang, C. Liu, F. Tsow, H. Yu, and N. Tao, "Noncontact monitoring breathing pattern, exhalation flow rate and pulse transit time,"

IEEE Transactions on Biomedical Engineering, vol. 61, no. 11, pp. 2760–2767, 2014.

[21] C. B. Pereira, X. Yu, V. Blazek, and S. Leonhardt, "Robust remote monitoring of breathing function by using infrared thermography," in *2015 37th Annual International Conference of the IEEE Engineering in Medicine and Biology Society EMBC*, 2015, pp. 4250–4253.

[22] J. Geisheimer and E. F. Greneker, "A non-contact lie detector using radar vital signs monitor RVSM technology," *IEEE Aerospace and Electronic Systems Magazine*, vol. 16, no. 8, pp. 10–24, 2001.

[23] A. Nezirovic, A. G. Yarovoy, and L. P. Ligthart, "Signal processing for improved detection of trapped victims using UWB radar," *IEEE Transactions on Geoscience and Remote Sensing*, vol. 48, no. 4, pp. 2005–2014, 2010.

[24] K. Higashikaturagi, Y. Nakahata, I. Matsunami, and A. Kajiwara, "Non-invasive respiration monitoring sensor using UWB-IR," in *2008 IEEE International Conference on Ultra-Wideband*, 2008, vol. 1, pp. 101–104.

[25] V. Petrini, V. Di Mattia, A. De Leo, P. Russo, V. Mariani Primiani, G. Manfredi, G. Cerri, and L. Scalise, "Ambient assisted living electromagnetic sensor for continuous breathing monitoring applied to movement analysis: a preliminary study," in *2014 IEEE/ASME 10th International Conference on Mechatronic and Embedded Systems and Applications MESA*, 2014, pp. 1–5.

[26] V. Petrini, V. Di Mattia, A. De Leo, P. Russo, V. Mariani Primiani, G. Manfredi, G. Cerri, and L. Scalise, "Domestic monitoring of respiration and movement by an electromagnetic sensor," in *Ambient Assisted Living*, 2015, pp. 133–142.

[27] L. Scalise, A. De Leo, V. M. Primiani, P. Russo, D. Shahu, and G. Cerri, "Non contact monitoring of the respiration activity by electromagnetic sensing," in *2011 IEEE International Workshop on Medical Measurements and Applications Proceedings (MeMeA)*, 2011, vol. 1, pp. 418–422.

[28] B. Allen, M. Dohler, E. Okon, W. Malik, A. Brown, and D. Edwards, *Ultra wideband antennas and propagation for communications, radar and imaging*, John Wiley & Sons, 2006.

[29] M. A Hanson, H. C. Powell Jr., A. T Barth, K. Ringgenberg, B. H. Calhoun, J. H. Aylor, , and J. Lach, "Body area sensor networks: Challenges and opportunities," *Computer*, vol. 42, no. 1, pp. 58, 2009.

[30] H. B. Lim, D. Baumann, and E. P. Li, "A human body model for efficient numerical characterization of UWB signal propagation in wireless body area networks," *IEEE transactions on Biomedical Engineering*, vol. 58, no. 3, pp. 689–697, 2011.

[31] K. Fujii, M. Takahashi, K. Ito, K. Hachisuka, Y. Terauchi, Y. Kishi, K. Sasaki, and K. Itao, "Study on the transmission mechanism for wearable device using the human body as a transmission channel," *IEICE transactions on communications*, vol. 88, no. 6, pp. 2401–2410, 2005.

[32] P. S. Hall, Y. Hao, Y. I. Nechayev, A. Alomainy, C. C. Constantinou, C. Parini, M. R. Kamarudin, T. Z. Salim, D. T. M. Hee, A. S. Owadally R. Dubrovka, W. Song, A. Serra, P. Nepa, M. Gallo, , and M. Bozzetti, "Antennas and propagation for on-body communication systems," *IEEE Antennas and Propagation Magazine*, vol. 49, no. 3, pp. 41–58, 2005.

[33] L. Roelens, S. Van den Bulcke, W. Joseph, G. Vermeeren, and L. Martens, "Path loss model for wireless narrowband communication above flat phantom," *Electronics Letters*, vol. 42, no. 1, pp. 10–11, 2006.

[34] L. Roelens, W. Joseph, E. Reusens, G. Vermeeren, and L. Martens, "Characterization of scattering parameters near a flat phantom for wireless body area networks," *IEEE Transactions on Electromagnetic Compatibility*, vol. 50, no. 1, pp. 185–193, 2008.

[35] "Cst - computer simulation technology," Available at: `http://www.cst.com`, Lastchecked February 2017.

[36] K. S. Kunz and R. J. Luebbers, *The finite difference time domain method for electromagnetics*, CRC press, 1993.

[37] C. K. Chou, H. Bässen, J. Osepchuk, G. Balzano, R. Petersen, M. Meitz, R. Cleveland, J. Lin, and L. Heynick, "Radio frequency electromagnetic exposure," *Journal of Bioelectromagnetics*, vol. 17, pp. 195–208, 1996.

[38] W. C. Gibson, *The method of moments in electromagnetics*, CRC press, 2014.

[39] A. Poston, "Human engineering design data digest: human factors standardization systems," *Human Factors Standardization SubTAG*, 2000.

[40] "Makehuman - open source tool for making 3d characters," Available at: `http://www.makehuman.org/`, Lastchecked February 2017.

[41] "Cst - computer simulation technology/simulation performance," Available at: `https://www.cst.com/products/cstmws/performance`, Lastchecked February 2017.

[42] C. A. Balanis, *Advanced engineering electromagnetics*, John Wiley & Sons, 2012.

[43] J. B. Keller, "Geometrical theory of diffraction," *JOSA*, vol. 52, no. 2, pp. 116–130, 1962.

[44] L. S. Pedrotti, *Basic geometrical optics*, Fundamentals of photonics, 2012.

[45] P. Ya. Ufimtsev, "Method of edge waves in the physical theory of diffraction," Tech. Rep., DTIC Document, 1971.

[46] J. M. Gutiérrez, L. J. A. Martínez, and F. L. Las Heras Andrés, *High frequency techniques: The physical optics approximation and the modified equivalent current approximation (MECA)*, InTech, 2011.

[47] C. J. Panagamuwa, W. G. Whittow, R. M. Edwards, and J. C. Vardaxoglou, "Experimental verification of a modified specific anthropomorphic mannequin SAM head used for SAR measurements," in *2007 Loughborough Antennas and Propagation Conference*, 2007, pp. 261–264.

[48] A. Arkko, "Properties of numerical SAM phantom used in mobile phone antenna simulations," in *2005 IEEE Antennas and Propagation Society International Symposium*, 2005, pp. 450–453.

[49] Y. Uno, K. Saito, M. Takahashi, and K. Ito, "Structure of cylindrical tissue-equivalent phantom for medical applications," in *2010 International Conference on Electromagnetics in Advanced Applications ICEAA*, 2010, pp. 406–409.

[50] T. Aoyagi, M. Kim, and J. Takada, "The utilization of body skeleton model for modeling the dynamic ban channels," in *2012 6th European Conference on Antennas and Propagation EUCAP*, 2012, pp. 540–543.

[51] C.M. Furse, J.Y. Chen, and O.P. Gandhi, "The use of the frequency-dependent finite-difference time-domain method for induced current and SAR calculations for a heterogeneous model of the human body," *IEEE Transactions on electromagnetic compatibility*, vol. 36, no. 2, pp. 128–133, 1994.

[52] D. Kurup, W. Joseph, G. Vermeeren, and L. Martens, "Specific absorption rate and path loss in specific body location in heterogeneous human model," *IET Microwaves, Antennas & Propagation*, vol. 7, no. 1, pp. 35–43, 2013.

[53] "Speag," Available at: `https://www.speag.com/products/em-phantom/overview`, Lastchecked February 2017.

[54] "Voxel-man," Available at:https://www.voxel-man.com, Lastchecked February 2017.

[55] N. Hassan, "The necessity of simulating the whole human body in studying the interaction between antennas and the body," in *ICCES 2009. International Conference on Computer Engineering & Systems.*, 2009, pp. 338–343.

[56] P. van Dorp and F. C. A. Groen, "Human walking estimation with radar," *IEE Proceedings-Radar, Sonar and Navigation*, vol. 150, no. 5, pp. 356–365, 2003.

[57] Nello Carrara, "Dielectric properties of body tissues," Available at: http://niremf.ifac.cnr.it/tissprop/htmlclie/htmlclie.php, Lastchecked February 2017.

[58] D. Andreuccetti and F. Roberto, "Proprietà dielettriche dei tessuti umani: definizioni, modello parametrico, codici di calcolo," *IEEE Transactions on Microwave Theory and Techniques*, vol. 54, no. 4, 2000, Centre National de la Recherche Scientifique.

[59] Lawrence R Rabiner and Ronald W Schafer, *Digital processing of speech signals*, Prentice Hall, 1978.

[60] "Mathworks - matlab," Available at: https://it.mathworks.com/products/matlab, Lastchecked February 2017.

[61] A. De Leo, P. V. Mariani, P. Russo, D. Shau, V. Di Mattia, and G. Cerri, "Breath detection of humans buried in a homogeneous lossy medium: a simplified analytical model," in *2012 International Symposium on Electromagnetic Compatibility (EMC EUROPE)*, 2012, pp. 1–6.

[62] Ł. Januszkiewicz and Sł. Hausman, "Simplified human phantoms for wireless body area network modelling," in *2015 9th European Conference on Antennas and Propagation EuCAP*, 2015, pp. 1–4.

[63] T. Zasowski, G. Meyer, F. Althaus, and A. Wittneben, "Propagation effects in UWB body area networks," in *2005 IEEE international conference on ultra-wideband*, 2005, pp. 16–21.

[64] T. Zasowski, G. Meyer, F. Althaus, and A. Wittneben, "UWB signal propagation at the human head," *IEEE Transactions on Microwave Theory and Techniques*, vol. 54, no. 4, pp. 1836–1845, 2006.

[65] J. S. Avestas, "The physical optics method in electromagnetic scattering," *Journal of Mathematical Physics*, vol. 21, no. 2, pp. 290–299, 1980.

[66] A. Akhmanov and S. Yu. Nikitin, *Physical optics*, Clarendon Press, 1997.

[67] T. Shijo, L. Rodriguez, and M. Ando, "The modified surface-normal vectors in the physical optics," *IEEE Transactions on Antennas and Propagation*, vol. 56, no. 12, pp. 3714–3722, 1980.

[68] C. A. Balanis, *Antenna theory: analysis and design*, John Wiley & Sons, 2016.

[69] S. Ramo, J. R. Whinnery, and T. Van Duzer, *Fields and waves in communication electronics*, John Wiley & Sons, 2008.

[70] P. W. Barber and C. Yeh, "Scattering of electromagnetic waves by arbitrarily shaped dielectric bodies," *Applied Optics*, vol. 14, no. 12, pp. 2864–2872, 1975.

[71] L. Scalise, V. Petrini, V. Di Mattia, P. Russo, A. De Leo, G. Manfredi, and G. Cerri, "Multiparameter electromagnetic sensor for AAL indoor measurement of the respiration rate and position of a subject," in *2015 IEEE International Instrumentation and Measurement Technology Conference I2MTC Proceedings*, 2015, pp. 664–669.

[72] V. Petrini, V. Di Mattia, G.Manfredi, A. De Leo, P. Russo, G. Cerri, and L. Scalise, "An electromagnetic contactless system for apnea monitoring," in *2016 IEEE International Conference on Smart Cities ISC2.*, 2016, pp. 1–4.

[73] R. Mavaddat, *Network scattering parameters*, World Scientific, 1996.

[74] J. D. Kraus, R. J. Marhefka, and A. S. Khan, *Antennas and wave propagation*, Tata McGraw-Hill Education, 2006.

[75] E. H. Braun, "Some data for the design of electromagnetic horns," *IRE Transactions on Antennas and Propagation*, vol. 4, no. 1, pp. 29–31, 1956.

[76] E. F. Knott, *Radar cross section measurements*, Springer Science & Business Media, 2012.

[77] B. R. Mahafza, *Radar systems analysis and design using MATLAB*, CRC press, 2002.

[78] N. Swathi, K. S. Ranga Rao, G. Sasibhushana Rao, N. Usha, and N. Sharma, "Radar rcs estimation of a perfectly conducting sphere obtained from a spherical polar scattering geometry," in *2015 International Conference on Electrical, Electronics, Signals, Communication and Optimization EESCO.*, 2015, pp. 1–7.

[79] C. G. Don and A. J. Cramond, "Creeping wave analysis of impulse propagation through a shadow boundary," *The Journal of the Acoustical Society of America*, vol. 80, no. 1, pp. 302–305, 1986.

[80] C. J. Roy, "Permittivity and measurements," *Encyclopedia of RF and microwave engineering*, 2005.

[81] J. M. Garcia-Rubia, O. Kilic, V. Dang, Q. M. Nguyen, and N. Tran, "Analysis of moving human micro-doppler signature in forest environments," *Progress In Electromagnetics Research*, vol. 148, pp. 1–14, 2014.

[82] Youngwook Kim and Hao Ling, "Human activity classification based on micro-doppler signatures using a support vector machine," *IEEE Transactions on Geoscience and Remote Sensing*, vol. 47, no. 5, pp. 1328–1337, 2009.

[83] J. L. Geisheimer, E. F. Greneker III, and W. S. Marshall, "High-resolution doppler model of the human gait," in *AeroSense 2002*, 2002, pp. 8–18.

[84] M. Otero, "Application of a continuous wave radar for human gait recognition," in *Defense and Security*, 2005, pp. 538–548.

[85] A. Ghaleb, L. Vignaud, and J. M. Nicolas, "Micro-doppler analysis of wheels and pedestrians in ISAR imaging," *IEE Proceedings-Radar, Sonar and Navigation*, vol. 150, no. 5, pp. 356–365, 2003.

[86] V. C. Chen and S. Qian, "Joint time-frequency transform for radar range-doppler imaging," *IEEE Transactions on Aerospace and Electronic Systems*, vol. 34, no. 2, pp. 486–499, 2003.

[87] O. Couderc, J. C. Cexus, F. Comblet, A. Toumi, and A. Khenchaf, "ISAR imaging based on the empirical mode decomposition time-frequency representation," in *International Radar Symposium 2016 (IRS2016)*, 2016.

[88] S. Hainsworth, M. Macleod, S. W. Hainsworth, and M. D. Macleod, "Time frequency reassignment: A review and analysis," *IEEE Transactions on Geoscience and Remote Sensing*, vol. 5, no. 1, pp. 177–204, 2003.

[89] C. J. Roy, "Grid convergence error analysis for mixed-order numerical schemes," *AIAA journal*, vol. 41, no. 4, pp. 595–604, 2003.

[90] L. Eça and M. Hoekstra, "Discretization uncertainty estimation based on a least squares version of the grid convergence index," in *Proceedings of the Second Workshop on CFD Uncertainty Analysis, Instituto Superior Tecnico, Lisbon, Oct*, 2006, p. 7.

[91] P. J. Roache, *Fundamentals of verification and validation*, hermosa publ., 2009.